Ultrasmall Manganese Ferrites for In Vivo Catalase Mimicking Activity and Multimodal Bioimaging

Susana Carregal-Romero, Ana Beatriz Miguel-Coello, Lydia Martínez-Parra, Yolanda Martí-Mateo, Pablo Hernansanz-Agustín, Yilian Fernández-Afonso, Sandra Plaza-García, Lucía Gutiérrez, María del Mar Muñoz-Hernández, Juliana Carrillo-Romero, et al.

Ultrasmall manganese ferrites for *in vivo* catalase mimicking activity and multimodal bioimaging

Susana Carregal-Romero,[a,b] Ana Beatriz Miguel-Coello,[a] Lydia Martínez-Parra,[a] Yolanda Martí-Mateo,[c] Pablo Hernansanz-Agustín,[c] Yilian Fernández-Afonso,[d,e,f] Sandra Plaza-García,[a] Lucía Gutiérrez,[d,e,f] María del Mar Muñoz-Hernández,[c] Juliana Carrillo-Romero,[a] Marina Piñol-Cancer,[a,b] Pierre Lecante,[g] Zuriñe Blasco-Iturri,[a] Lucía Fadón,[a,h] Ana C. Almansa-García,[a] Marco Möller,[a] Dorleta Otaegui,[a] Jose Antonio Enríquez,[c,i] Hugo Groult,[j] Jesús Ruíz-Cabello[a,b,k,l*]*

S. Carregal-Romero, A-B. Miguel-Coello, L. Martínez-Parra, S. Plaza-García, J. Carrillo-Romero, M. Piñol-Cancer, Z. Blasco-Iturri, L. Fadón, A. C. Almansa-García, M. Möller, D. Otaegui, J. Ruíz-Cabello
Center for Cooperative Research in Biomaterials (CIC biomaGUNE), Basque Research and Technology Alliance (BRTA), 20014 San Sebastián, Spain
E-mail: scarregal@cicbiomagune.es, jruizcabello@cicbiomagune.es

S. Carregal-Romero, M. Piñol-Cancer, J. Ruíz-Cabello
CIBER de Enfermedades Respiratorias (CIBERES), 28029 Madrid, Spain

Y. Martí-Mateo, P. Hernansanz-Agustín, M. Muñoz-Hernández, J. Antonio Enríquez
Centro Nacional de Investigaciones Cardiovasculares Carlos III (CNIC), 28029 Madrid, Spain

Y. Fernández-Afonso, Lucía Gutiérrez
Departamento de Química Analítica, Universidad de Zaragoza, 50009 Zaragoza, Spain
Instituto de Nanociencia y Materiales de Aragón (INMA), CSIC-Universidad de Zaragoza, 50009 Zaragoza, Spain
Centro de Investigación Biomédica en Red de Bioingeniería, Biomateriales y Nanomedicina (CIBER-BBN), 50009 Zaragoza, Spain

P. Lecante
CEMES-CNRS, Université de Toulouse, UPR 8011 CNRS, 31055 Toulouse, France

L. Fadón
Center for Cooperative Research in Bioscience (CIC bioGUNE), Building 800, Science and Technology Park of Bizkaia, 48160 Derio, Spain

J. Antonio Enríquez
Centro de Investigación Biomédica en Red de Fragilidad y Envejecimiento Saludable (CIBERFES), 28029 Madrid, Spain

H. Groult
BCBS team (Biotechnologies et Chimie des Bioressources pour la Santé), LIENSs Laboratory (Littoral environment et Sociétés), UMR CNRS 7266, 17000 La Rochelle, France

J. Ruíz-Cabello
Ikerbasque, Basque Foundation for Science, 48013 Bilbao, Spain
Departamento de Química en Ciencias Farmacéuticas, Universidad Complutense de Madrid, 28040 Madrid, Spain

Keywords: manganese ferrite nanoparticles, magnetic resonance imaging, positron emission tomography, catalase-mimicking catalysis, hypoxia alleviation

Manganese ferrite nanoparticles display interesting features in bioimaging and catalytic therapies. They have been recently used in theranostics as contrast agents in magnetic resonance imaging (MRI), and as catalase-mimicking nanozymes for hypoxia alleviation. These promising applications encourage the development of novel synthetic procedures to enhance the bioimaging and catalytic properties of these nanomaterials simultaneously. Herein, a cost-efficient synthetic microwave method has been developed to manufacture ultrasmall manganese ferrite nanoparticles as advanced multimodal contrast agents in MRI and positron emission tomography (PET) and improved nanozymes. Such synthetic method allows doping ferrites with Mn in a wide stoichiometric range ($Mn_xFe_{3-x}O_4$, $0.1 \leq x \leq 2.4$), affording a library of nanoparticles with different magnetic relaxivities and catalytic properties. These tuned magnetic properties give rise to either positive or dual-mode MRI contrast agents. On the other hand, higher levels of Mn doping enhance the catalytic efficiency of the resulting nanozymes. Finally, through their intracellular catalase-mimicking activity, these ultrasmall manganese ferrite nanoparticles induce an unprecedented tumor growth inhibition in a breast cancer murine model. All of these results show the robust characteristics of these nanoparticles for nanobiotechnological applications.

1. Introduction

Manganese ferrite nanoparticles (MFNPs) have garnered increasing interest in the field of nanomedicine as theranostic agents due to their Fenton/Haber-Weiss catalytic properties (acting as catalase-mimicking nanozymes), their ability to produce contrast on magnetic resonance imaging (MRI), and their capability to produce heat.[1-4] On the one hand, these nanoparticles (NPs) can consume hydrogen peroxide intracellularly, producing oxygen for catalytic therapy.[1, 3, 5, 6] They can directly interact with intracellular H_2O_2-mediated signaling pathways and balance the concentration of O_2 and reactive oxygen species (ROS) known to be related to the failure of some regenerative medicines and the pathogenesis of diseases such as cancer or lung fibrosis.[7-10] This brings therapeutic opportunities such as enhancing the therapeutic effect of traditional anticancer therapies (*e.g.*, chemotherapy or photodynamic therapy), thanks to their H_2O_2 depletion and O_2 generation within the hypoxic and H_2O_2-rich microenvironment of the tumor.[3, 11] Recently, nanovesicles composed of densely packed manganese ferrite nanoparticles have also been applied for hypoxia alleviation in cutting-edge anticancer therapies such as sonodynamic and

chemoimmunotherapy.[12, 13] Currently, the ROS/O_2 balance is being targeted by many advanced manganese ferrite NP-based therapies that have become a relevant tool in nanobiotechnology.[1, 5, 11]

On the other hand, MFNPs can produce heat after exposure to alternating magnetic fields for hyperthermia and act as contrast agents for MRI due to their magnetic properties.[14-16] Magnetic hyperthermia is not efficient for ultrasmall MFNPs due to their low specific absorption rate.[17] However, these size-dependent physicochemical properties can be used strategically to improve MRI contrast.[2] Iron oxide nanoparticles, typically used as efficient T_2 contrast agents, can only behave as T_1 contrast agents when their size is below 5 nm.[18, 19] Indeed, in this case the size-dependent enhancement of r_1 relaxivity of the ultrasmall IONP is normally accompanied by an r_2 relaxivity decrease and a consequent strong reduction of T_2 contrast ability.[20] Contrary, ultrasmall manganese ferrite (UMFNPs) with a size below 5 nm also shows a good T_1 contrast but keep as well an appropriate transversal relaxivity for negative contrast T_2.[16, 20] This allows performing dual contrast imaging T_1/T_2, which is sought for reducing imaging artifacts in MRI and improving their performance compared to ultrasmall IONP.[21] Conventional single-mode T_1 or T_2 imaging can produce misleading results due to image artifacts, such as those happening in calcified tissues holding endogeneous T_1 contrast.[21] Hence, dual contrast T_1/T_2 agents based on materials such as doped iron oxides are considered the most promising substitutes of the gold standard Gd chelates.[21-23]

Typically, producing UMFNPs with dual T_1/T_2 contrast requires time-consuming synthetic protocols, organic solvents, temperatures (~ 200ºC), and additional purification steps to obtain ready-to-use water-soluble nanoparticles.[16, 23, 24] In this research work, taking a fast microwave-assisted method, we demonstrate that it is possible to produce ready-to-use water-soluble UMFNPs that are simultaneously highly efficient as MRI contrast agents and as catalase-mimicking nanozymes. Additionally, this synthesis allows core-radiolabeling for positron emission tomography (PET) contrast, which broadens the application of these UMFNPs in bioimaging. We develop a robust, one-pot synthetic protocol that provides UMFNPs with variable Mn doping ($Mn_xFe_{3-x}O_4$, $0.1 \leq x \leq 2.4$) through modifying the Mn/Fe ratio in the reaction conditions. Interestingly, the synthetic reaction's conditions also caused remarkable differences in the Mn doping level, and its adjustment allowed better control of the Mn incorporation yield. By tailoring the UMFNPs chemical composition, it was possible to

customize magnetic relaxivity values of r_1 and r_2 for dual-mode T_1/T_2 MRI contrast and the catalase-mimicking activity.[3, 16] To our knowledge, comparative studies that correlate catalytic behavior, MRI contrast, and UMFNP stoichiometry are scarce, and this information may benefit the optimization of UMFNPs for practical nanobiotechnological applications. Moreover, we demonstrate the UMFNP's performance as novel multimodal MRI/PET bioimaging agents *in vivo,* providing information about the NP's biodistribution, and showing the remarkable effect of this kind of NPs as tumor growth inhibitors in a breast cancer murine model.

2. Results and Discussion

2.1. Synthesis of UMFNPs

2.1.1. Microwave-Assisted Synthetic Protocol of UMFNPs

There are four bottom-up methods for preparing ferrites and iron oxide NPs using well-differentiated wet chemistry: hydrolytic (co-precipitation and hydrothermal), organic, and polyol.[24-26] Although organic or polyol methods usually have multiple synthetic steps and are not time and cost-efficient, they are mostly preferred to hydrolytic methods because both co-precipitation and hydrothermal methods have a reputation for providing highly polydisperse NPs.[2, 14] However, recently, microwave-assisted hydrolytic methods with controlled pressure and temperature have demonstrated that it is possible to produce water-soluble ferrites with well-controlled size and magnetic properties in one-pot.[27-29] Because these syntheses can be ultrafast, it is possible to rapidly functionalize the NP surface and modify the magnetic core with radioisotopes to perform multiple assays, including nuclear imaging with short-lived radioisotopes, ideal for clinical applications, as we have recently published for iron oxide NPs.[30, 31] To demonstrate that microwave-assisted hydrolytic syntheses are optimal methods to produce monodisperse UMFNPs with controlled tailoring of Mn stoichiometry (x, in $Mn_xFe_{3-x}O_4$), we prepared two series of NPs using an increasing ratio from 0.05 to 6 of *[Mn]/[Fe]* precursors. UMFNPs were synthesized at 240 W and 100 ºC for 10 min in an aqueous solution (2.5 mL) of iron trichloride hexahydrate ($FeCl_3 \cdot 6H_2O$) and manganese dichloride tetrahydrate ($MnCl_2 \cdot 4H_2O$) at different *[Mn]/[Fe]* ratios and a fixed amount of citric acid (20 mg) and hydrazine (250µL). We assayed two different reaction conditions, with or without HCl (P1 and P2 respectively), an acid already used to dope iron oxide nanoparticles with other metals, to study its influence on the incorporation of Mn.[31] The absence/presence of HCl in the

reaction mixture yielded the following pH during the synthetic reaction: a) 10.6 (protocol P1) and b) 9.1 (protocol P2). Overall, this led to two series of UMFNPs, respectively named as follows: i) MnFe1-MnFe7 (protocol P1) and ii) $^{H+}$MnFe8-$^{H+}$MnFe14 (protocol P2). **Figure 1** shows a schematic representation of the synthesis that allows tailoring the UMFNP composition and an example of transmission electron microscopy (TEM) and high-resolution TEM (HRTEM) images of one of the obtained UMFNPs (more images can be found in **Figure S1-S2**).

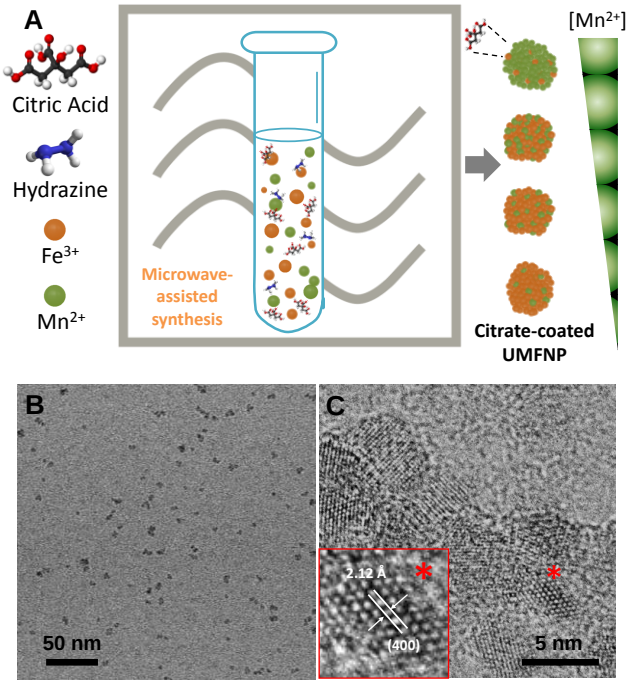

Figure 1. A) Schematic representation of the microwave-assisted method used to produce citrate-coated UMFNPs with fine control in the chemical composition. B) TEM and C) HRTEM images of citrate-coated $Mn_{0.95}Fe_{2.05}O_4$ ($^{H+}$MnFe11) and $Mn_{0.63}Fe_{2.38}O_4$ (MnFe4) respectively produced in the one-pot microwave-assisted synthesis. The inset shows the lattice fringes of the selected NP (*) with a bottom side of 3.8 nm.

2.1.2. Tailored Mn Doping Level of UMFNPs

Table 1 gathers the chemical formula $Mn_xFe_{3-x}O_4$ determined from inductively coupled plasma mass spectrometry (ICP-MS) for all the UMFNPs synthesized with the two different protocols (P1, P2) at increasing reaction ratios *[Mn]/[Fe]*. To further confirm the stoichiometry of UMFNPs, we performed an elemental analysis with different techniques (**Figure S3-S6, Table S1**). All UMFNPs analyzed with X-ray photoelectron spectroscopy (XPS) confirmed the presence of O, Mn, Fe, and C, the main components of the citrate-coated UMFNPs, and the intensity increase of the Mn

2p peak (and the subsequent intensity decrease of the Fe 2p peak) for synthesis with increasing reaction ratios *[Mn]/[Fe]*. These results indicate that one can tailor the Mn doping level in a wider range from $0.1 \leq x \leq 2.4$ using our P2 microwave-assisted synthetic protocol compared with P1 and other reported MFNPs. [4, 24] **Figure 2A and Table 1** compare the obtained $x_{measured}$ values with the theoretical Mn stoichiometry value $x_{theoretical}$, considering a reaction yield of 100 % for similar precursor ratios of *[Mn]/[Fe]*. Interestingly, we found that by incorporating HCl in the synthetic reaction mixture, the Mn yield was higher than 50 % regardless of the *[Mn]/[Fe]* ratio (**Figure 2B**). Contrariwise, the absence of acid drives to significantly lower Mn yields, especially at higher $x_{measured}$, hindering the increase of the Mn stoichiometry above x= 1.5. However, it is still unclear how the HCl presence at a concentration of *[HCl]*= 0.02 M can affect Mn's incorporation.

Table 1. Synthetic parameters and theoretical vs. measured Mn stoichiometries (x). The standard deviations are obtained by comparing the values obtained from different sample batches.

Sample	Abbr.	$[Mn]/[Fe]_{(i)}$	x theoretical	x measured
$Mn_{0.15}Fe_{2.85}O_4$	MnFe1	0.12	0.32	0.15±0.01
$Mn_{0.30}Fe_{2.70}O_4$	MnFe2	0.34	0.75	0.30±0.03
$Mn_{0.50}Fe_{2.50}O_4$	MnFe3	0.68	1.23	0.50±0.03
$Mn_{0.62}Fe_{2.38}O_4$	MnFe4	1.09	1.57	0.62±0.02
$Mn_{1.01}Fe_{1.99}O_4$	MnFe5	2.50	2.14	1.01±0.04
$Mn_{1.15}Fe_{1.85}O_4$	MnFe6	3.72	2.35	1.15±0.16
$Mn_{1.37}Fe_{1.63}O_4$	MnFe7	5.97	2.57	1.37±0.14
$Mn_{0.14}Fe_{2.86}O_4$	$^{H+}$MnFe8	0.05	0.15	0.14±0.004
$Mn_{0.35}Fe_{2.65}O_4$	$^{H+}$MnFe9	0.12	0.32	0.35±0.04
$Mn_{0.51}Fe_{2.49}O_4$	$^{H+}$MnFe10	0.20	0.50	0.51±0.02
$Mn_{0.95}Fe_{2.05}O_4$	$^{H+}$MnFe11	0.51	1.00	0.95±0.05
$Mn_{1.38}Fe_{1.62}O_4$	$^{H+}$MnFe12	1.09	1.50	1.38±0.04
$Mn_{1.83}Fe_{1.17}O_4$	$^{H+}$MnFe13	1.99	2.00	1.83±0.22
$Mn_{2.42}Fe_{0.58}O_4$	$^{H+}$MnFe14	6.02	2.57	2.42±0.04

* SD of the mean of n (n=3) independent syntheses. (i) initial concentration ratio. MnFe1-MnFe7 (black letters) have been produced with protocol P1, and MnFe8-MnFe14 (grey letters) have been produced with protocol P2.

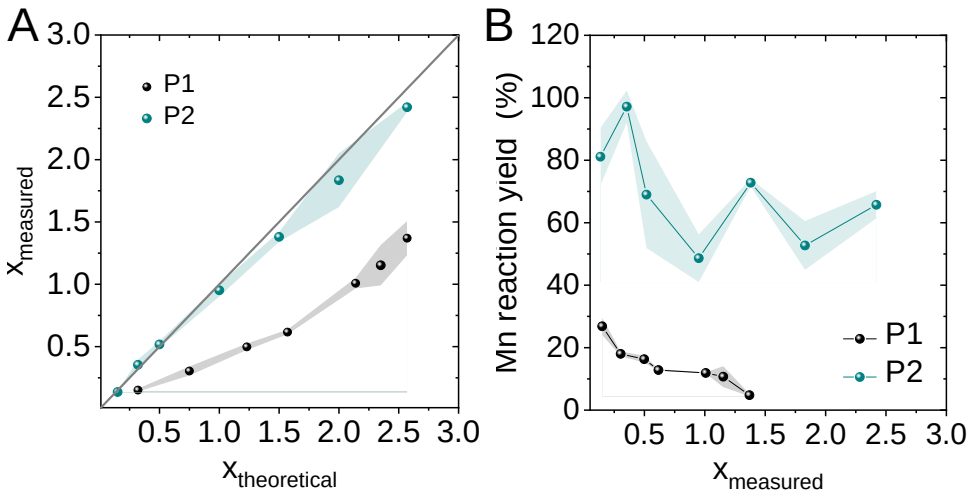

Figure 2. (A) Theoretical Mn stoichiometry *x* (gray line) considering a reaction conversion of 100% of precursor's initial concentration compared to *x*, measured by ICP-MS for the P1 and P2 synthetic protocols. (B) Mn incorporation yield in UMFNPs produced with two synthetic protocols P1 and P2.

As far as we know, the increase of pH alone has only been reported to increase the size of iron oxide NPs, rather than influencing their transition metals doping level.[32] In our protocol, it is clear that HCl might be influencing the formation mechanism of UMFNPs due to the different chemical compositions obtained with similar precursor ratios *[Mn]/[Fe]*. In ferrites doped with Zn^{2+}, Szczerba et al. suggested that this type of metal doping disparities arise from differences in the sub nano/atomic structure.[33] For inverse spinel structures, they determined that slightly different synthetic protocols allow the metal dopant to occupy both the octahedral O_h and tetrahedral T_d positions, while other protocols only allow the divalent metal cation to be in T_d positions. These distinct doping levels were associated with differences in the NP nucleation and growth mechanism of doped ferrites, but the key parameters that made it possible remain elusive. In our synthetic method, hydrazine is added in one-pot to an aqueous solution of citric acid, $FeCl_3$, and $MnCl_2$. In this first step, hydrazine N_2H_4 rapidly hydrolyzes to hydrazinium $(N_2H_5)^+$ (and OH^-), which reduces Fe^{3+} to Fe^{2+}.[32] The Mn^{2+} and Fe^{2+} ions react with dissolved oxygen and hydroxyl ions to form intermediate metal oxides that condense and turn into more stable and definitive spinel structures.[32, 34] The addition of HCl in P2 can affect in three directions: decreasing the reducing capacity of hydrazine, limiting the OH^- concentration, and forming iron complexes with chloride anions such as $[Fe(OH_2)_5Cl]^{2+}$.[35-37] However,

a detailed study on the reaction mechanism would be required beyond this work to determine the key parameters that rule the Mn incorporation in UMFNPs.

2.2. Characterization of UMFNPs

All UMFNPs were characterized by TEM and dynamic light scattering to obtain the core and the hydrodynamic sizes and the zeta potential of the nanoparticles (**Table S2**). **Figure 3A** indicates a relative homogeneity of the UMFNP core diameter d_{TEM} (3.9 nm on average) obtained with TEM regardless of the incorporation level of Mn and the absence/presence of HCl (P1 or P2 protocol). Interestingly, the presence of HCl slightly decreases the hydrodynamic diameter d_h (**Figure 3B**) and improves the hydrodynamic size distribution (**Figure S7**).

To study the citrate-coating of the UMFNPs, we performed thermogravimetric analysis (TGA) and obtained combustion profiles (**Figure 3C**) similar to other reported citrate-coated NPs.[29] Their loss of mass corresponding to a thick citrate coating was between 30 to 40 % up to 600°C. Interestingly, when comparing the number of citrate molecules per NP, the obtained results determined that UMFNPs (both in P1 and P2) with higher Mn stoichiometry contained higher amounts of citrate molecules on their surface (**Figure S8**). This increase of the coating shell for higher doping degrees was already observed for Cu-doped ferrites and could affect the magnetic and relaxometric properties of UMFNPs.[38] Besides, TGA results confirmed that P1 UMFNPs have a higher number of citrate molecules in their coating than P2 which can explain the DLS results in **Figure 3B** and **Table S2**.

The crystallinity of all UMFNPs was studied with HRTEM, wide-angle x-ray scattering (WAXS) and Raman spectroscopy. We observed with HRTEM clear lattice fringes, as shown in **Figures 1C and S2**. The observed lattice spacings of 2.12Å, 2.45 Å, 2.56 Å, and 3.01 Å could correspond to the (400), (222), (311), and (220) of the lattice planes that would be in good agreement with the inverse spinel structure of standard manganese ferrite nanocrystals.[2, 39] However, due to the small size of nanoparticles, WAXS analysis was more accurate to determine the crystallinity/amorphization of the UMFNPs series. **Figure 3D** shows the WAXS profile for the P2 UMFNP series compared with the magnetite's reported scattering pattern. Visibly, the crystalline structure sticks to the inverse spinel structure of Fe_3O_4, with no significant change in crystalline parameters for Mn stoichiometries below x= 1.4. Contrary, nearly full amorphization was obtained for the UMFNPs with $x \geq 1.4$.

Interestingly, when comparing P1 and P2 UMFNPs, a higher degree of crystallinity was observed for P2 UMFNPs (**Figure 3E**). However, for both kinds of UMFNPs, the corresponding radial distribution function (*RDF*) analysis, shown in **Figure S9**, determined a similar crystalline domain size steadily close to 3 nm and a drop in amplitude between $^{H+}$MnFe10 (x= 0.51) and MnFe3 (x= 0.50) consistent with the decrease of crystallinity between P2 and P1 UMFNPs. To go further in the description of the Mn doped cores, we performed XRD (**Figure S10**) which confirmed magnetite structure for UMFNPs, and Raman spectroscopy on selected UMFNPs from the library with Mn doping between x=0.1 and 0.5 (**Figure S11A,B**). Raman spectra were recorded at 532 nm excitation at a low intensity to avoid any heat-induced formation of hematite and different spots were scanned to reflect the homogeneity of the samples. The pattern of nanosized magnetite spinel was clearly found in all the NPs.[40] Especially the typical peak of A1g vibration mode was found around 675 cm^{-1}, and two bands centred around 350 cm^{-1} and 500 cm^{-1} can be reasonably attributed to Eg and T2g mode, respectively. In the case of UMFNPs obtained with P1, presence of mixed maghemite phase was also identified by the characteristic shoulder of the A1g vibration mode around 700 cm^{-1}. Surface oxidation on Fe_3O_4 nanoparticles has indeed often been reported.[41, 42] Interestingly, this shoulder had a much lower intensity and was barely detectable for the NPs achieved with P2, traducing a higher purity of the magnetite cores obtained in more acidic condition (**Figure 3F**). In all cases, the presence of Mn cations in the structure was verified with the broadening of the A1g band to the lower frequency towards 600 cm^{-1}, linked with their preferential substitution at the tetrahedral sites.[43, 44] Broad peaks and complex spectrum in the 250-550 cm^{-1} may also suggest substitution at the octahedral sites and/or oxidation. However, it was difficult to detect a gradual effect along with Mn doping increase. Raman spectra performed on $^{H+}$MnFe13 with higher Mn content (x= 1.83) revealed appearance on an intense peak at 590 cm^{-1}, confirming partially inverted spinel lattice in this case (**Figure S10C**).

The Mn doping level, size, coating, the presence of secondary phases, and crystallinity of UMFNPs strongly influence the magnetic properties of UMFNPs. To study them, field-dependent magnetization, *M(H)*, hysteresis curves were recorded at 300 K. All UMFNPs showed a superparamagnetic behavior with very small remnant magnetization and coercive field values (**Figure S12**) at this temperature. Saturation magnetization (M_s) values from all the characterized NPs ranged between 1 and 45

Am^2/kg ferrite. These values were in all cases lower than those of other bigger manganese ferrites NPs reported in the literature (particle diameter ≈ 8 nm, M_s between 60 and 75 Am^2/kg) and the bulk stoichiometric $MnFe_2O_4$.[24, 45] In the past, and using a similar synthetic approach, we have previously described that undoped iron oxide NPs of similar sizes (≈ 4 nm) and coating, like the ones reported here, usually present M_s values (down to 20 Am^2/kg)[29] below the typical values for bulk magnetite or maghemite (92-100 or 60-80 Am^2/kg respectively) due to the small particle sizes obtained by this synthetic approach.[46] Thus, due to a size effect, the generally low M_s values reported for these UMFNPs could be explained. Nevertheless, although with slight deviations, the general tendency for both synthetic protocols was that M_s values decreased with increasing levels of Mn doping (*x*) (**Figure 3G**). Previous works studying the saturation magnetization values of manganese ferrite NPs had reported this same trend of decreasing M_s values for increasing levels of Mn doping up to molar ratios of [Mn]/[Fe]≈ 0.2, which corresponds to $x \approx 0.5$.[14, 24, 47] A tendency to obtain increasing M_s values from 0.2 molar ration onwards was described in some of these previous results. However, the maximum Mn stoichiometry only reached ≈ 0.45 Mn/Fe molar ratio, much lower than the around 4 molar ratio obtained here for the sample with the highest amount of incorporated Mn ($^{H+}$MnFe 14, x =2.4, molar ratio ≈ 4). In our case, we do not observe this "V" behavior on the *M(H)* vs. *x* results, and, in contrast, a decrease of the M_s values with the Mn doping is observed for all the range of studied x values.

Interestingly, only the sample with the highest amount of Mn ($^{H+}$MnFe14, *x*= 2.42) presented a paramagnetic contribution observed in the *M(H)* curves at the highest fields. To verify this contribution, the temperature dependence of the AC magnetic susceptibility was measured for selected samples (**Figure 3H**). All the samples presented the typical magnetic relaxation phenomenon of magnetic nanoparticles, with a maximum in the in-phase susceptibility (χ') accompanied by a maximum at slightly lower temperatures for the out-of-phase susceptibility (χ''). We confirmed that $^{H+}$MnFe14 also presented a paramagnetic contribution, observed at low temperatures, in the χ'(T) data. The existence of secondary phases with a paramagnetic contribution would have an impact on the saturation magnetization values calculated, however it was only detected in the sample with the highest Mn amount One of the possibilities to explain this paramagnetic contribution could be manganese oxide formation during the

synthesis. The XPS elemental analysis of the Mn 2p core level shows a satellite peak compatible with MnO (**Figure S4, S5, and S6**). Another more remote possibility could be the potential cation leaching that has been recently described during water transfer protocols.[24] However, this paramagnetic contribution has not been observed in any of the other characterized samples, so probably the formation of paramagnetic manganese oxide due to the highest Mn concentration used during the synthesis is a more plausible explanation of this paramagnetic signal.

Finally, a key aspect for any application of UMFNPs in the nanobiotechnological field is their colloidal stability in complex media. Due to their size, NPs are typically metastable (due to short-range van der Waals attraction) which can lead to undesirable agglomeration.[29] To avoid it, a coating agent can introduce steric or electrostatic repulsion to stabilize the NPs. In order to decipher the stability of the citrate-coated UMFPNs, we have followed the stability in terms of hydrodynamic size (**Figure 3I**) of these UMFNPs during several days at 37 ºC in a variety of buffers and solvents often used as cell culture media or for *in vivo* NP administration: a) nanopure water, b) saline solution (0.9 % NaCl), c) PBS buffer, pH 7.4, 5 mM, d) bovine serum albumin (BSA) 800 μM dissolved in PBS buffer, pH 7.4, 5 mM and d) cell culture Dulbecco's Modified Eagle's Medium (DMEM) supplemented with 10% fetal bovine serum (FBS) and 1% penicillin and streptomycin.[48] Note that in the protein-containing media, the hydrodynamic diameter of the protein-coated UMFNPs was sufficiently larger than the protein size (see **Figure S13**A).[49] The results show that UMFNPs were stable up to 24h in all media. However, salts and pH 7.4 induced agglomeration when the incubation times were t > 1-2 days. In nanopure water, UMFNP suspensions were stable at least for 5 days. The presence of proteins in the media (BSA or FBS) stabilized the NPs in complex media such as DMEM, as reported for citrate-coated Au NPs.[50] Colloidal stability was studied for both P1 and P2 UMFNPs obtaining similar results. We also freeze-dried the UMFNPs and demonstrated colloidal stability after redispersion in water solutions ensuring their long self-life (**Figure S13B,C**).[51] Therefore, the prepared UMFNPs have high colloidal stability, and it could be assumed that intravenous administration might not trigger NP agglomeration, at least to a large extent.[48]

In conclusion, our microwave-assisted synthesis method allows producing a library of magnetic and colloidally stable UMFNPs around 4 nm with variable Mn stoichiometry, crystallinity, and magnetic properties. Improving the Mn doping strategy

with the P2 protocol leads to better crystallinity and a slight decrease in the hydrodynamic ratio and polydispersity.

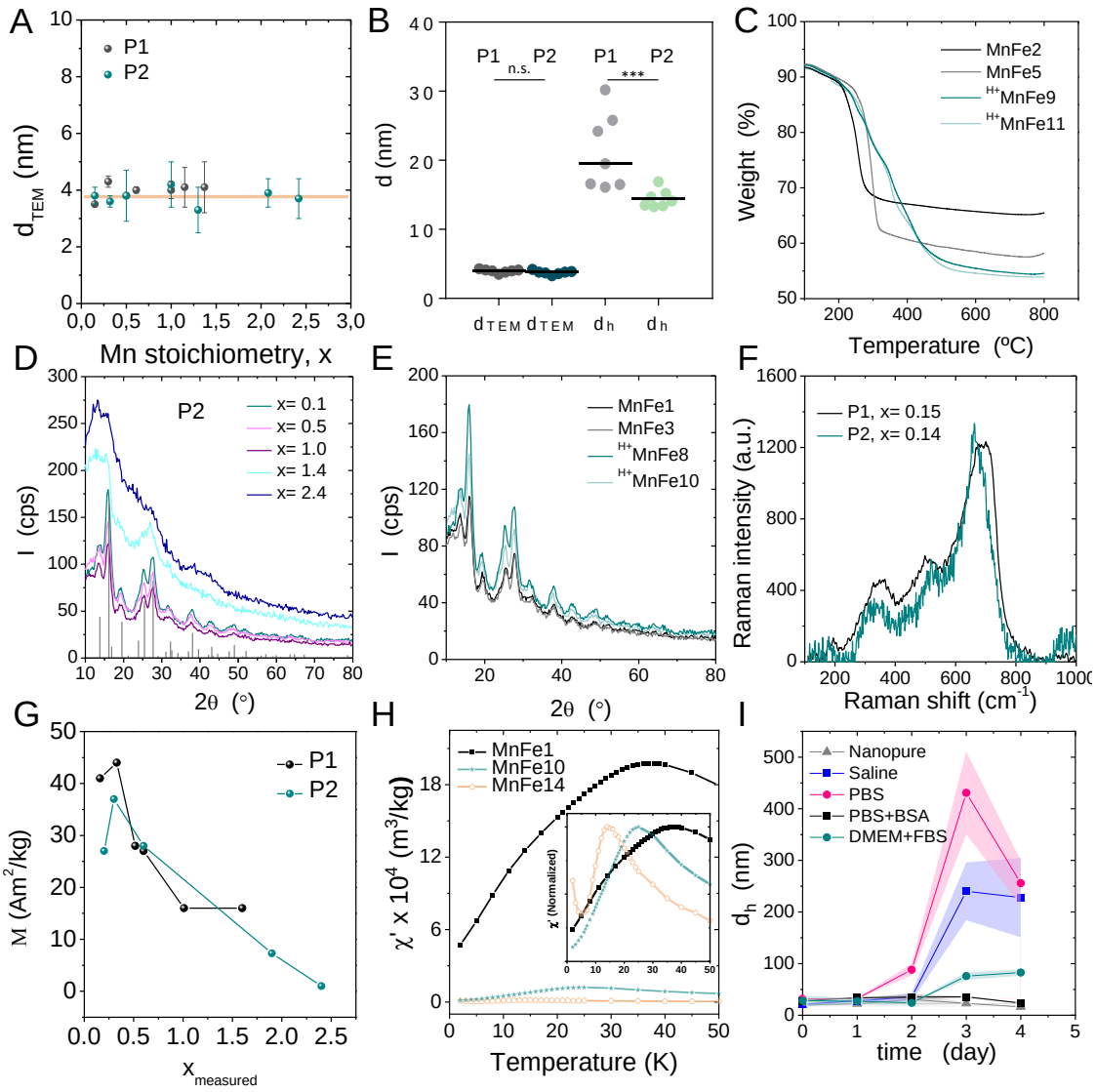

Figure 3. (A) Core diameter of UMFNPs with different Mn stoichiometry *x* produced with protocols P1 and P2. The orange line represents the average size of all prepared UMFNPs (3.9 nm). (B) Core and hydrodynamic diameter differences between the synthetic protocols determined by TEM (d_{TEM}) and DLS (d_h). (C) TGA combustion curves of UMFNPs obtained with P1 or P2 and with x ≈ 0.3 (MnFe2 and $^{H+}$MnFe9) and x ≈ 1 (MnFe5 and $^{H+}$MnFe11). (D) WAXS profile for P2 UMFNPs series as compared with magnetite (grey peaks). (E) Comparison of WAXS profile for UMFNPs prepared with P1 (MnFe1-3) and P2 ($^{H+}$MnFe8-10) and similar *x* value (□0.1 and □0.5, respectively). (F) Comparison between Raman spectra of MnFe1 and $^{H+}$MnFe8 as example to highlight their different atomic structure. (G) Saturation magnetization

values as a function of the Mn doping (x) calculated from field-dependent magnetization measurements at 300 K. (H) Temperature dependence of the in-phase magnetic susceptibility of selected samples. In the inset, data had been scaled to their maxima to compare better the position in temperature and the presence of a paramagnetic contribution easily observed for $^{H+}$MnFe14 at low temperature. (I) Colloidal stability of UMFNPs (this plot corresponds to MnFe6) at different time points in different solutions: (▲) water, (■) saline (0.9 % NaCl), (●) PBS at pH 7.4, (■) PBS supplemented with BSA (800 μM), and (■) cell culture media DMEM supplemented with 10% FBS and 1% of penicillin and streptomycin.

2.3. Setting Up T_1/T_2 Contrast Efficiency by Tailoring Mn Stoichiometry

To evaluate the feasibility of the UMFNPs library as efficient T_1 ($1<r_2/r_1<3$), T_2 ($r_2/r_1>10$) or dual-mode T_1/T_2 ($3<r_2/r_1<10$) MRI-based contrast agents, their relaxometric properties were measured with a 1.5 T relaxometer (**Figure 4A-D**) and a 7 T preclinical MRI scanner (**Figure 4D and S14**). First, we observed for the UMFNP obtained with different protocols P1 and P2 (**Figure 4B and 4C**) the impact of Mn's presence within the ferrite compared with undoped ultrasmall iron oxide NPs (IONP) produced with similar synthesis (d< 5nm, r_2/r_1= 2.34), suitable for T_1 contrast.[29] Both the T_1 and T_2 contrast ability improved with a slight Mn doping ($x \approx 0.15$) as compared with IONP (x= 0), from r_1= 6.8 and r_2= 15.9 mM^{-1} s^{-1} for IONP to r_1= 8.8 ± 0.7, r_2= 22.8 ± 1.7 mM^{-1} s^{-1} for MnFe1 (x= 0.15, P1) and r_1= 10.4 ± 1.7, r_2= 24.8 ± 3.9 mM^{-1} s^{-1} for $^{H+}$MnFe8 (x= 0.14, P2). Overall, this enhancement improved the ability of the UMFNPs to perform efficient T_1 contrast, reflected by the r_2/r_1 values that are maintained below 3 (**Figure 4D**). Additionally, the r_1 values obtained at 1.5 T with UMFNPs of $x < 0.6$ were excellent compared with gold standard MRI T_1 contrast agents such as Gadovist or Resovist with r_1= 3.3 and 8.7 s^{-1} mM^{-1} respectively, showing that they can be promising candidates as T_1 contrast agents.[52] At higher Mn content ($x \geq 0.6$), and due to the variation of both relaxation times r_1 and r_2, the relaxivity ratio r_2/r_1 value ($3<r_2/r_1<10$) falls in a regime where UMFNPs can be suitable for dual-mode T_1/T_2 MRI contrast. This possibility of dual-mode appears as a new feature in comparison to undoped ultrasmall IONP and bigger MFNPs.[3]

All the observed trends in the r_1 and r_2 (**Figure S14A**) relaxivity values for P1 and P2 UMFNPs, obtained at 1.5 T, were reproduced and confirmed with a 7 T scanner (**Figure 4E and Figure S14B**). We have determined that the Mn^{2+} doping in UMFNPs

can enhance both the r_1 and r_2 relaxivities compared with ultrasmall IONP, as previously reported.[20, 39] However, the effect of increasing the Mn stoichiometry from 0.1 to 2.4 revealed a complex contribution between the inner-sphere and outer-sphere. As core size, known to have a major influence on these two models, were similar for all the nanoparticles, this complexity has been associated with an independent impact of both contributions to ultrasmall nanoparticle's relaxivities compared to their larger counterparts.[39]

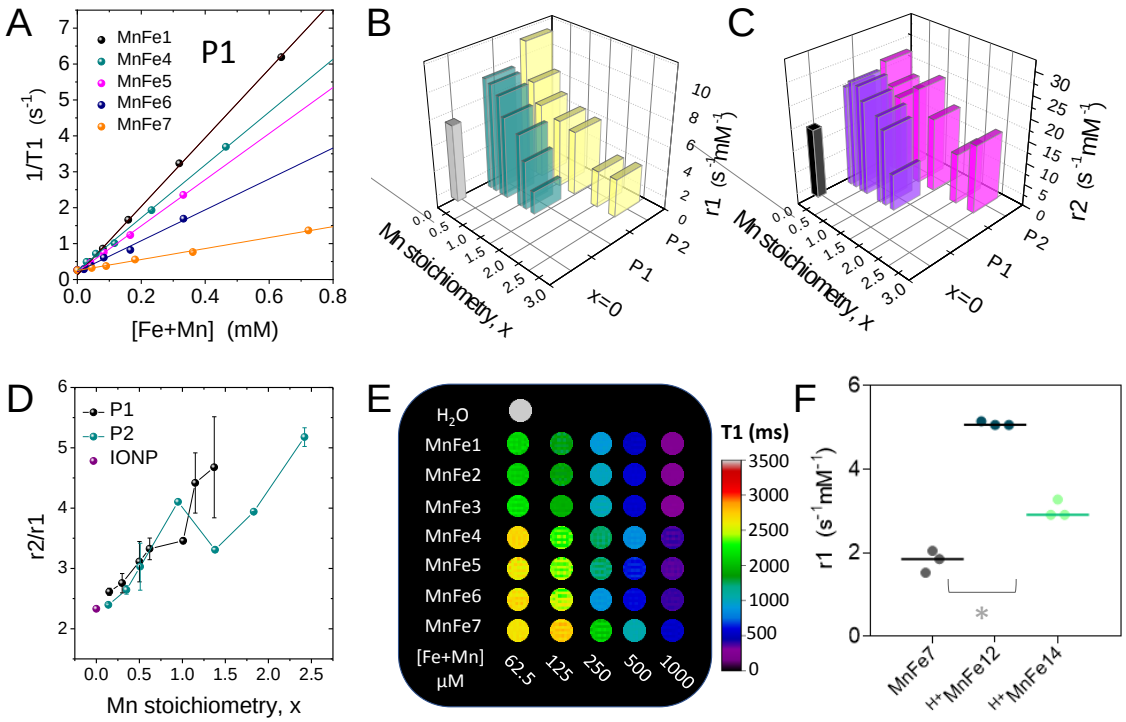

Figure 4. (A) T_1 relaxation rates of P1 UMFNPs with variable Mn stoichiometry. (B) r_1 relaxivities measured in 1.5 T relaxometer of P1 UMFNPs (green) and P2 UMFNPs (yellow) compared with r_1 of undoped IONPs (grey bar). (C) r_2 relaxivities measured in 1.5 T relaxometer of P1 UMFNPs (violet) and P2 UMFNPs (pink) compared with r_2 of undoped IONPs (black bar). (D) Comparison of r_2/r_1 relaxivity ratios between P1 and P2 UMFNPs. (E) 7 T MRI T_1 contrast of P1 UMFNPs with increasing Mn stoichiometry. (F) Statistical analysis (Dunn's multiple comparison test) of the difference in r_1 value between MnFe7 (x=1.4, P1) prepared with P1 and $^{H+}$MnFe12 and $^{H+}$MnFe14 (x= 1.4 and 1.8, P2).

The inner-sphere relaxation contribution is due to the direct coordination of water molecules from the solution to the surface metal ions of the NPs. This relaxation contribution r_1 has been reported to increase with higher Mn^{2+} doping levels in

manganese ferrites because Mn cations provide a lower residence lifetime of bound water on the NP surface.[2] However, the r_1 is also highly influenced by the crystallinity of the NP, and its coating density, thickness, and composition. Probably this explains that the increase of Mn^{2+} doping in our ultrasmall NPs triggered a decrease of r_1 due to the decrease of crystallinity and increased coating density.

The outer-sphere relaxation is due to the spin-spin interactions between the UMFNPs and the bulk water molecules in the nearby environment. This contribution is highly dependent on the saturation magnetization M_s between other parameters, such as the core size. **Figure 3G** showed the decrease of M_s with higher Mn doping levels, which can partially explain the r_2 reduction.

Therefore, the observed r_1 and r_2 changes by increasing Mn stoichiometry are likely to be caused to a large extent by the increase of coating thickness and the decrease of crystallinity and the M_s. These facts partially screen the effect of augmenting the Mn doping level leading to a decrease of both r_1 and r_2. This behavior has already been reported for UMFNPs with a Mn stoichiometry between 0.7 and 1.6 and Cu-doped ferrites. However, the mechanism of T_1/T_2 contrast tailoring by chemical engineering of UMFNPs remains unclear.[2, 38]

Finally, we studied the difference in relaxometric properties between the synthetic protocols. We compared the specific r_1 and r_2 values of each UMFNP obtained with the P1 and P2 protocols and determined that for most ferrites, the values were similar for a given *x*, with no statistically significant differences. Only when **x**≥1.4, the r_1 and r_2 relaxivities of MnFe7 (P1) were significantly lower ($P<0.05$) than those obtained with its counterpart $^{H+}$MnFe12. These values were similar to $^{H+}$MnFe14, which has *x*= 2.4 (**Figure 4F and S14C**). This effect could be due to the thicker citrate coating measured of P1 UMFNPs compared with P2 UMFNPs. Additionally, the r_2/r_1 ratios presented in **Figure 4D** showed that for both types of NPs, r_2/r_1 is below 3 for $x \leq 0.5$ and $3 \leq r_2/r_1 \leq 10$ for UMFNPs with $x \geq 0.6$, leading to a similar ability as dual-mode contrast agents. This means that for both protocols P1 and P2, the *x* value is the main parameter determining whether NPs are good T_1 contrast agents or can also be considered dual-mode T_1/T_2 contrast agents.

Due to the small differences in the relaxometric properties observed for NPs manufactured with different protocols, we can conclude that P1 and P2 UMFNPs are excellent T_1 or dual-model T_1/T_2 contrast agents. Only P1-UMFNPs with high Mn content ($x \geq 1.4$) present significantly lower r_1 and r_2 values and reduced capabilities for

positive MRI contrast. Interestingly, most of the obtained r_1 and r_2 values were similar to the relaxometric values obtained with UMFNPs prepared with well-known organic synthesis, confirming that microwave-assisted methods are suitable for producing efficient MRI contrast agents based on UMFNPs.[2, 16]

2.4. Multimodal Bioimaging and Biodistribution

2.4.1. Cytotoxicity

Before evaluating UMFNPs for *in vivo* applications, the biosafety of the UMFNPs was assessed *in vitro* (in blood and cell cultures) and *in vivo* in C57BL/6JRj mice after intravenous (i.v.) UMFNP administration. For this, we first conducted blood hemolysis assays with selected UMFNPs produced with the two different protocols (**Figure S14**). The results obtained showed hemolysis between 4.3 and 13.3 % for MnFe7 (x= 1.37) and between 3.6 and 10.0 % for $^{H+}$MnFe9 (x= 0.35) with no significant differences between the range of concentrations assayed and the negative control. According to previous studies, the percent hemolysis is rated as "no concern" below 25 %.[53] Therefore, our UMFNPs are blood compatible. Then, cell viability assays were conducted in lung carcinoma epithelial A549 cells and healthy embryonic fibroblast NIH-3T3 cells in presence of UMFNPs covering the whole range of Mn doping levels obtained ($0.1 \leq x \leq 2.4$) at different incubation times (24, 48 and 72 h) and concentrations between 0.1 and 50 μg/mL (**Figure S15**). Results obtained with A549 cells indicated a low influence of UMFNPs on cell viability. However, in the case of the NIH-3T3 cell line, high UMFNP concentrations up to 50 μg/mL generate a decrease of cell viability, especially at long incubation times (72h). Interestingly, this effect on NIH-3T3 viability correlates with higher manganese content in the ferrite NP (**Figure S15**). Finally, to evaluate UMFNP innocuousness further, we also performed a histopathological analysis in C57BL/6JRj mice after their i.v. administration (**Figure S16**). Following the 3Rs principle in animal experimentation and because P2-UMFNPs have the broadest Mn stoichiometry ($0.14 \leq x \leq 2.42$), we only assayed *in vivo* the biosafety of NPs produced from this protocol. The histopathological examination determined similar low inflammation scores (1, from 0 to 3) for the liver of untreated and i.v.- administered UMFNPs. These results agree with already reported biosafety studies of manganese ferrite NPs.[2, 16]

2.4.2. In vivo MRI and Biodistribution

The *in vivo* performance of UMFNPs as dual-mode T_1/T_2 contrast agents and the corresponding NP biodistribution of UMFNPs was evaluated with two kinds of NPs, which hold both apparent low cytotoxicity but have different Mn stoichiometry ($^{H+}$FeMn9 (x= 0.35) and $^{H+}$FeMn11 (x= 0.95)) and different relaxivity values. During the imaging sessions, anatomical images were acquired before and after UMFNP administration to appropriately allocate the organs of interest. The quantification of the NP biodistribution was carried out by analyzing longitudinal and transversal T_1 and T_2 parametric maps (**Figure 5**) from acquired multi-echo images of animals at four different time points before and after i.v. administration. This study was performed in groups of n=3 animals, and T_1 and T_2 values were measured in selected regions of interest (ROIs) for all organs avoiding the inclusion of regions with high relaxivity values, which may correspond to fluids like blood or bile. Both kidneys were analyzed separately (right and left) and selected three different ROIs; total, cortex, and medulla, to avoid misleading results in the analysis. **Figure 5** summarizes the obtained T_1 and T_2 parametric maps of animals and the corresponding mean relaxation T_1 and T_2 values (n= 3) pooling together all the pre- and post-contrast points. The organs of the two main clearance routes of NPs from the bloodstream, the reticuloendothelial and urinary system, showed some UMFNP accumulation. A detailed MRI analysis determined that both $^{H+}$FeMn9 (x= 0.35) and $^{H+}$FeMn11 (x= 0.95) behaved as efficient dual T_1/T_2 MRI contrast agents. $^{H+}$FeMn11 NPs induced higher differences of T_1 and T_2 after administration and thus higher contrast than $^{H+}$FeMn9, probably due to higher r_2/r_1 values (**Figure S18, Table S3**). Regarding the biodistribution of the two kinds of UMFNPs, we observed from T_1 and T_2 decrease that they both accumulated in similar organs right after i. v. administration: liver, spleen, and kidneys.

Interestingly, the dual T_1/T_2 contrast possibility provided complementary information about the fate of our UMFNPs in these organs after 24h. The T_1 analysis showed a recovery of the T_1 signal after 24h in all tissues (**Table S3**). This change could indicate either the clearance of UMFNPs from these organs or a fast NP degradation. If a fast renal clearance through the urine is likely to occur, it is known that NPs are not rapidly eliminated from the liver.[54] In this case, when confined in hepatic macrophages, the r_1 value of magnetic NPs has been reported to decrease significantly while the r2 value increase because of aggregation, leading overall to a higher r_2/r_1 ratio and T_2 governing the MRI contrast.[55-57] Indeed, in solution, we verified a larger

decrease of r_1 than r_2 in agglomerated UMFNPs driven by high ionic strength. The T_2 analysis in the liver showed a time-dependent and long-lasting decrease for the two probes.

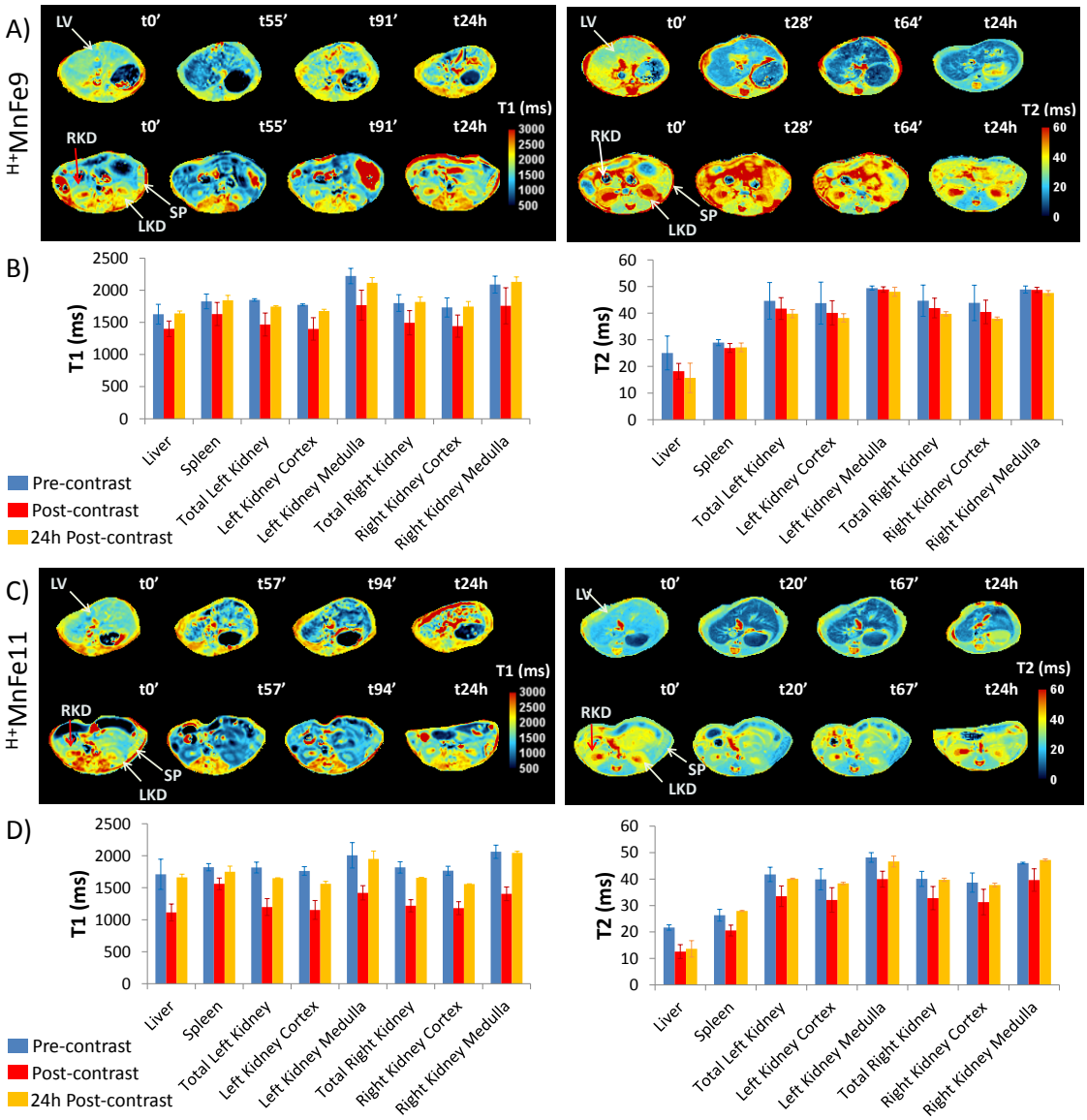

Figure 5. *T_1* and *T_2* relaxation maps (A, C) at two different locations of the abdomen of a mouse showing the liver (LV) at the top rows in both images and the spleen (SP) and the right and left kidneys (RKD, LKD) at the bottom row in both images. Four different time points are presented to reflect the changes in *T_1* and *T_2* values before (*t*0′) and additional minutes/hours after the intravenous injection of $^{H+}$MnFe9 (A, *x*= 0.35) and $^{H+}$MnFe11 (C, *x*=0.95) UMFNPs. (B, D) Mean (± SD) *T_1* and *T_2* relaxation values obtained for different organs pre- (blue), post- (red) injection and (yellow) 24h post-injection of the $^{H+}$MnFe9 (B) and $^{H+}$MnFe11 (D) UMFNPs.

To confirm these results, histological and mass spectrometry determinations of Fe and Mn in the liver were performed 24h after the i.v. administration. Results in Figure 6 demonstrated the presence of UMFNPs of both kinds of NPs in the liver at 24h. Interestingly, the mass spectrometry analysis of Mn in the liver determined a 2.8 fold increase of Mn in mice administered with $^{H+}$FeMn11 compared with $^{H+}$FeMn9, precisely consistent with the 2.7 fold increase of Mn between these two probes (x= 0.95 and 0.35, respectively). Histological samples stained with Perl's Prussian blue showed small blue dots corresponding with Fe^{3+} in agglomerated UMFNPs with sizes below 10 µm.

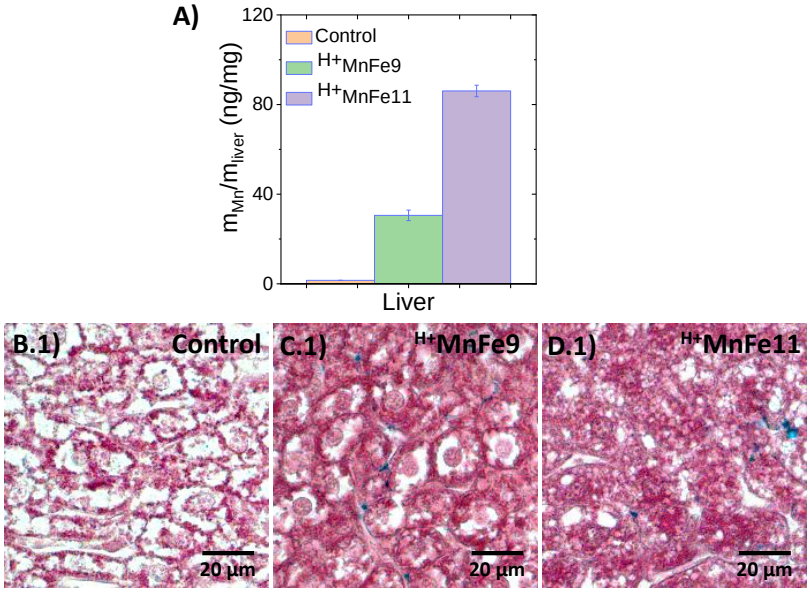

Figure 6. *Ex vivo* determination by ICP-MS of Mn accumulation in the liver after 24h. The mass of Mn was determined for a dried mass of the liver. (A) Histological determination of the UMFNPs presence in the liver (B.1-D.1) and kidneys (B.2-D.2) by Perl's Prussian blue staining of Fe^{3+}. B, C, and D correspond to tissues from control mice (not administered with UMFNPs) administered with $^{H+}$FeMn9, and $^{H+}$FeMn11, respectively.

Overall, It seems that we are detecting the time point of massive accumulation of our UMFNPs after being uptaken by hepatic macrophages thanks to the advantages that offer the dual-mode T_1/T_2-MRI contrast. This effect of "turn on/off" the T_1 or T_2-MRI contrast due to a biological trigger can be applied in visualizing precise therapies as reported.[58] and it is an advantage over non-doped ultrasmall IONP.

2.4.2. Radiolabelling and PET Biodistribution

Positron emission tomography combined with computed tomography (PET/CT) is the most sensitive technique for rapid quantifiable NP biodistribution analysis.[59] *In vivo* quantification of the accumulation of NPs in the different organs is not possible with MRI. However, MRI is a better option for soft-tissue imaging. Therefore, the combination of MRI/PET/CT is compelling for multidimensional molecular imaging.[30] Here, we demonstrate that UMFNPs with tailored Mn stoichiometry (*x*= 0.31, 1.15, and 2.54) are easily core-doped with traces of ^{68}Ga for positron emission tomography (PET) as we have previously demonstrated for undoped ultrasmall iron oxide NPs.[30] This radioisotope has a short half-life of 1.1285 h which minimizes the radiation dose and allows characterizing the nanoparticles few days after the synthesis. The obtained radiolabeling yield was 65 %, 55 % and 10 % corresponding to UMFNPs with x= 0.31, 1.15, and 2.54 respectively.

The physicochemical characterization of the radiolabeled UMFNPs (x= 0.31, 1.15, and 2.54) prepared with protocol P2 (with enhanced metal doping) showed (see **Figure S19**, **Table S4, S5, and S6**) a negligible influence on the core size (3.8, 4.1 and 3.5 nm), zeta potential (-13.4, -23.6 and -19 mV), and hydrodynamic ratio (14, 11.6 and 17.4 nm) as compared to cold UMFNPs. Regarding the MRI contrast properties, we determined a slight decrease of the magnetic relaxivities. Contrary, a slight increase of the catalytic activity was observed for radiolabeled UMFNPs compared to cold UMFNPs.

We studied the biodistribution of only one of the radiolabeled UMFNPs to demonstrate their performance as PET contrast agents ($^{68Ga}Mn_{0.31}Fe_{2.69}O_4$, r_1 = 5.85 s^{-1} mM^{-1} and r_2 = 9.33 s^{-1} mM^{-1} and TOF = 0.009 min^{-1}). Thanks to its radiolabeling with ^{68}Ga, it was possible to determine that these citrate-coated UMFNPs remained in the circulation after one hour of intravenous administration. About 10 % of the ID/cm^3 was still present in the bloodstream after 60 minutes. These results are consistent with our previous work with citrate-coated ultrasmall iron oxide NPs.[60]

In **Figure 7**, PET experiments also showed that UMFNPs are cleared from the bloodstream through mainly the liver, bladder, and kidneys. This confirms the MRI results and shows that UMFNPs tended to be trapped in the liver and spleen, the mononuclear phagocytic system's main organs. However, a substantial amount of UMFNPs are first cleared by the kidneys and subsequently excreted by the urine, which

explains the increased activity value in the bladder, reaching 10 % after one hour. The analysis of urine (**Figure S20**) by PET, gamma counting, and ICP-MS also demonstrates the presence of the metallic components of UMFNPs: 68Ga, Mn and Fe. To finally confirm the partial renal excretion of UMFNPs, we measured the magnetic relaxivity of the extracted urine. This experiment evidenced the presence of magnetic nanoparticles due to the lowering of the relaxation times T_1 and T_2 (3.38 s, 2.74 s) respect to water (3.85 s, 3.36 s). Although the renal clearance threshold is about 6 to 8 nm, this biodistribution and clearance mechanism is typical of NPs with a hydrodynamic size between 10-20 nm at the limit between hepatic elimination and renal filtration.[60-62]

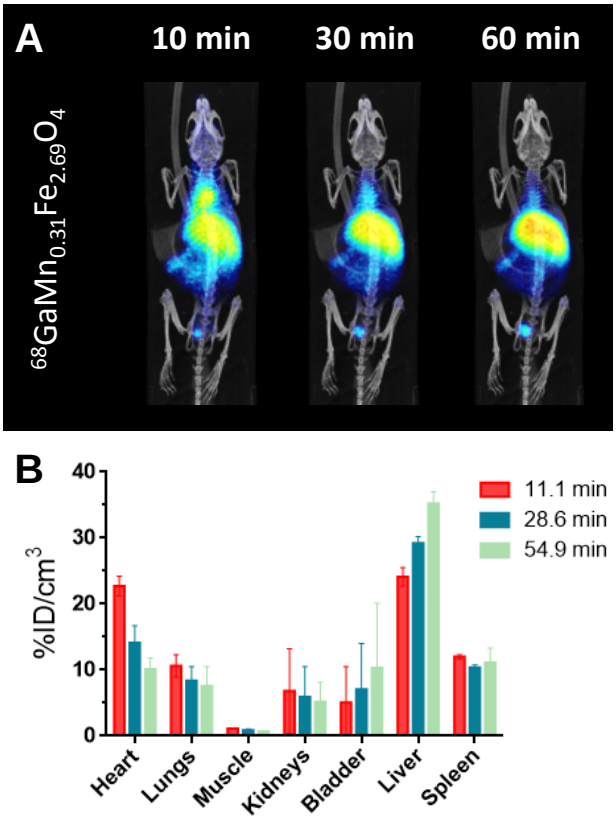

Figure 7. *In vivo* biodistribution study. (A) PET images at different time points of ^{68}Ga-UMFNPs (x=0.31). (B) *In vivo* quantification of the biodistribution at different time points of the ^{68}Ga-UMFNPs in the main organs (n=2).

2.5. Catalase-Mimicking Activity of UMFNPs

2.5.1. Parameters Influencing the Catalytic Activity of UMFNPs

Tumor hypoxia is known to decrease the efficiency of many nanomedicines.[63] To alleviate such lack of oxygen in the tumor microenvironment, nanoparticles such as

$Mn_1Fe_3O_4$ (x= 1) have been incorporated into the nanomaterial's toolbox to catalyze the oxygen production through the Fenton/Haber-Weiss reaction (**Figure 8A**).[1, 3, 5, 11] To demonstrate the catalytic properties of UMFNPs herein synthesized, were first incubated the nanoparticles with H_2O_2 and monitored the reaction time courses through an enzyme-based colorimetric assay (see Materials & Methods). **Figure 8B** shows that 100% of H_2O_2 was depleted in 70 min using 0.53 mM of MnFe7 (x= 1.38) and 0.8 mM of H_2O_2. Then, we linearized such reaction course with equation 1;

$$-\ln\frac{A_t - A_\infty}{A_o - A_\infty} = k_{obs}t \qquad (1)$$

where k_{obs} is the catalytic rate measured experimentally, A_o is H_2O_2 initial concentration, A_∞ is H_2O_2 at the end of the reaction, and A_t is the H_2O_2 at each time point. Such linearization evidenced that the kinetics of H_2O_2 consumption follows a first-order reaction with an observed catalytic constant of k_{obs}= 0.04 s^{-1}, R^2= 0.998. The same rate law was previously reported by Valdés-Solís et al. and others.[64] When we scaled the H_2O_2 concentration in the reaction up to 51 mM, we calculated a total turnover number (*TTN*: mol of H_2O_2 depleted per mol of catalyst) of 96 (**Figure S21**). When the *TTN* was divided by the reaction time to calculate the turnover frequency (*TOF*), the optimal Mn stoichiometry (x= 2.42) gave rise to a TOF value of roughly 0.07 min^{-1}. This number is one of the highest ever reported in the state of the art of manganese ferrites (**Table S7**). *TTN* and *TOF* values endorse the extraordinary catalytic potential of UMFNPs for biomedical applications.

Then, we studied the effect of the Mn stoichiometry of UMFNPs on the catalase-mimicking activity. First, **Figure 8C** shows that the higher Mn/Fe ratio in the UMFNPs, the higher their catalytic activity. The O_2 generation also increases with the Mn doping level (**Figure 8D**). Additionally, we demonstrate the continuous O_2 production after several H_2O_2 additions (**Figure 8E**) in different media. We observed that the O_2 generation rate was higher in cell culture media than in water, suggesting that the protein corona formation on NPs and the complex media enhances their catalytic properties.

To our knowledge, the impact of Mn doping on the catalase-mimicking catalytic activity of UMFNPs has not been reported yet. However, few studies have previously described the enhancement of the Fenton catalytic activity of manganese ferrites with increasing Mn stoichiometry (x=0.2-0.5 and x=0.7-1.2).[55, 65, 66] Although the

reaction mechanism of Fenton oxidation is still not fully understood, it has been reported that the limiting step in the Fenton reaction is H_2O_2 oxidation. In ferrites doped with Mn atoms, a remarkable increase of the H_2O_2 depletion is observed due to the *in situ* Mn reduction that boosts the Fenton reaction.[66] Hence, we suggest that UMFNPs also entail such a mechanism to transform H_2O_2 into O_2 more efficiently as the doped Mn atom increases the first Fenton activity in the Fenton/Haber-Weiss mechanism.

We also compared how the synthetic method (P1 or P2) affects the catalytic activity of UMFNPs. Although the two synthetic protocols slightly influenced magnetic and imaging features, their catalytic behavior was significantly different. **Figure 8F** illustrates that the P2 protocol allows synthesizing UMFNPs whose initial rate linearly increased as a function of the x value. On the contrary, the P1 protocol generates UMFNPs whose initial rates reached a plateau at $x \geq 0.5$. Furthermore, P1 UMFNPs are significantly more active than P2 UMFNPs at *x* values lower than 1.5. Since both kinds of NPs have similar sizes, different coatings (thinner for P2) may explain the catalytic dissimilarities for UMFNPs with similar *x*. However, the coating characterization (**Figure 3**) discards such a hypothesis. A more plausible explanation is the generation of different atomic structures when UMFNPs are synthesized through either P1 or P2 protocols with identical Mn stoichiometry. As Fe and Mn atoms can occupy tetrahedral (T_d) and octahedral (O_h) sites in the atomic inverse spinel structure of UMFNPs, but the O_h sites are the most catalytic ones due to their surface exposure.[56] Therefore, a synthetic protocol (i.e., P1 at low Mn (*x*) or P2 at high Mn (*x*)) that promotes the insertion of Mn^{2+} at O_h positions will produce more catalytically efficient UMFNPs. In agreement with our results, Mn^{2+} in O_h sites has been reported to accelerate the initial H_2O_2 depletion to produce □OH species and a more efficient regeneration of the active Fenton/Haber-Weiss Fe^{2+}species.[65] Therefore, different Mn occupancies and atomic organization might play a key role in the catalytic activity of P1 as compared to P2 UMFNPs (see **Figure 8F**). Further experiments with advanced techniques such as X-ray absorption near-edge structure (XANES) would be required to precisely determine the percentage of Mn and Fe atoms in T_d or O_h sites and their impact on the catalytic activity.[14]

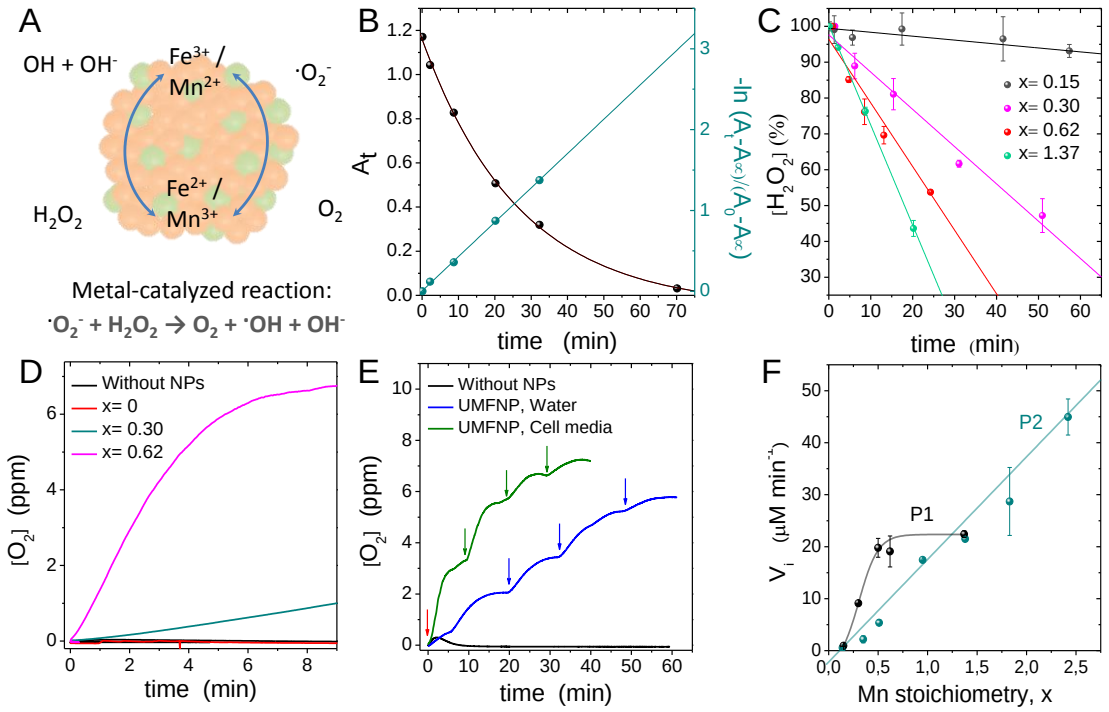

Figure 8. (A) Schematic representation of the Fenton/Haber-Weiss catalysis by UMFNPs. (B) Kinetic trace of the absorbance at 414 nm during the H_2O_2 decomposition by MnFe7 (x= 1.38) UMFNPs and fitting to first-order exponential decay (left y-axis, k_{obs}= 0.04 s^{-1}, R^2= 0.998) and the linearized data for first-order analysis (right y-axis, k_{obs}= 0.04 s^{-1}, $\underline{R}^2$= 0.999). (C) Temporal conversion of H_2O_2 catalyzed by UMFNPs with increasing Mn doping levels. (D) Comparison of O_2 generation catalyzed by UMFNPs with different Mn doping levels (0, 0.30, and 0.62) produced with P1. (E) Example of several H_2O_2 additions (4, pointed with an arrow) of O_2 generation performed by $^{H+}$MnFe11 (x= 0.95) in water and cell media. (F) Comparison of initial velocities of H_2O_2 consumption by UMFNPs produced with different synthetic protocols P1 and P2. All reaction kinetics have been performed with constant values of: $[Mn_xFe_{(3-x)}O_4]$= 0.53 mM, $[H_2O_2]$= 0.8 mM at room temperature.

2.5.2. Intracellular Catalysis and Antitumoral Effect in vivo

Once we characterized the catalytic performance of UMFNPs in a non-biological environment, we studied the performance of these nanoparticles to catalyze the Fenton/Haber-Weiss reaction in the cell milieu. To that aim, we first studied how UMFNPs alter the intracellular ROS concentration by incubating the nanoparticles with A549 lung carcinoma cells for 24h. Confocal laser scanning microscope (CLSM) images and plate reader fluorescence measurements revealed that UMFNPs with higher

Mn doping levels decreased intracellular ROS concentration (**Figure S22**). However, the ROS fluorescence probe used in the first term - the DCFH – fails to conclude that the ROS drop was due to the catalytic depletion of H_2O_2 since such probe is sensitive to both peroxides and radical species. To unambiguously confirm that UMFNPs were depleting the intracellular H_2O_2, we incubated that ROS probe in the presence of the intracellular free radical scavenger (N-(2-Mercaptopropionyl) glycine).[57] Pleasantly, we observed the decrease in the fluorescence signal that confirms the depletion of the intracellular H_2O_2 concentration (**Figure 9A**) triggered by UMFNPs. Besides the H_2O_2 depletion, the Fenton/Haber-Weiss reaction also generates hydroxyl radical species (□OH). We performed a mitochondrial hydroxyl radical detection assay to confirm whether they were formed during the intracellular UMFNPs catalysis (see Materials & Methods).[67] As a result, we found a subtle intracellular concentration increase of □OH due to their interaction with UMFNPs (**Figure 9B**). Although □OH is a highly potent oxidant that can degrade organic and inorganic molecules producing cell damage, we observed a negligible effect on cell cytotoxicity after incubation with UMFNPs (**Figure S16**). The short half-life of such radical (≈1 ns) precludes its participation in the intracellular signaling pathways that lead to cell death.[68]

Finally, we investigated whether UMFNPs affect intracellular hypoxia-inducible factor (HIF-1α) stabilization. This oxygen-sensitive subunit becomes stabilized in hypoxia and triggers cell signaling pathways that induce changes in the tumor microenvironment, ultimately favoring cancer progression (**Figure 9C**).[69, 70] Cells were incubated with and without UMFNPs under a hypoxic atmosphere (1.5% O_2, 5% CO_2, and 93.5% N_2) for several hours, and the degree of hypoxic signaling activation was assessed based on HIF-1α levels. Western blot analysis shows that HIF-1α decreased dramatically when cells were incubated with a nanoparticle concentration of 10 μg/mL, suggesting that UMFNPs can generate O_2 intracellularly and consequently alleviate hypoxia. All in all, these *in vitro* results demonstrate the intracellular properties of the UMFNPs-driven catalysis and their potential use as catalase-mimicking nanozymes for therapeutic applications.[65]

To complete the multidisciplinary journey, we tested the therapeutic potential of UMFNPs as nanomedicine in a breast cancer murine model. We selected $^{H+}$MnFe11 as its stoichiometry (x≈1) has been extensively used in combined anticancer therapies and do not have a therapeutic effect alone. Because the pH of the tumor microenvironment has been recorded to be mainly in the range of 6.4-7,[71] we first verified that this

UMFNPs were catalytic at acidic pHs such as 5.8 and 6.6 (**Figure S23A**) and barely dissolved under a pH of 5.8 (**Figure S23B**). Then, UMFNPs were i.v. administered to mice (n= 6) with the breast cancer tumor model induced with E0771 cells.[72] Through an ICP-MS analysis of tumor biopsies, we found UMFNPs within this tissue likely due to the enhanced permeability and retention (EPR) effect (**Figure 9E**).[73] After treatment, the tumor volume growth was longitudinally measured and compared with a control group (*n*=6) administered with a saline solution. After 6 days, we observed a moderate tumor growth inhibition (**Figures 9G and E**) conducting to a total tumor mass and HIF 1-α activity decrease (**Figures S23B, C, D, and E**) for those mice treated with UMFNPs. We further evaluated the *in vivo* toxicity by monitoring body weight loss after treatment. These results (**Figures S23F**) showed that UMFNPs were well tolerated, since no significant weight loss was observed in those animals treated with UMFNPs compared to the controls.

Unlike other studies where MFNPs were combined with other drugs to observe a therapeutic effect,[1, 3] this is the first demonstration of a standalone therapeutic potential of UMFNPs for cancer treatment. The excellent catalytic properties of these nanoparticles support a seemly hypoxia-mediated therapeutic effect.

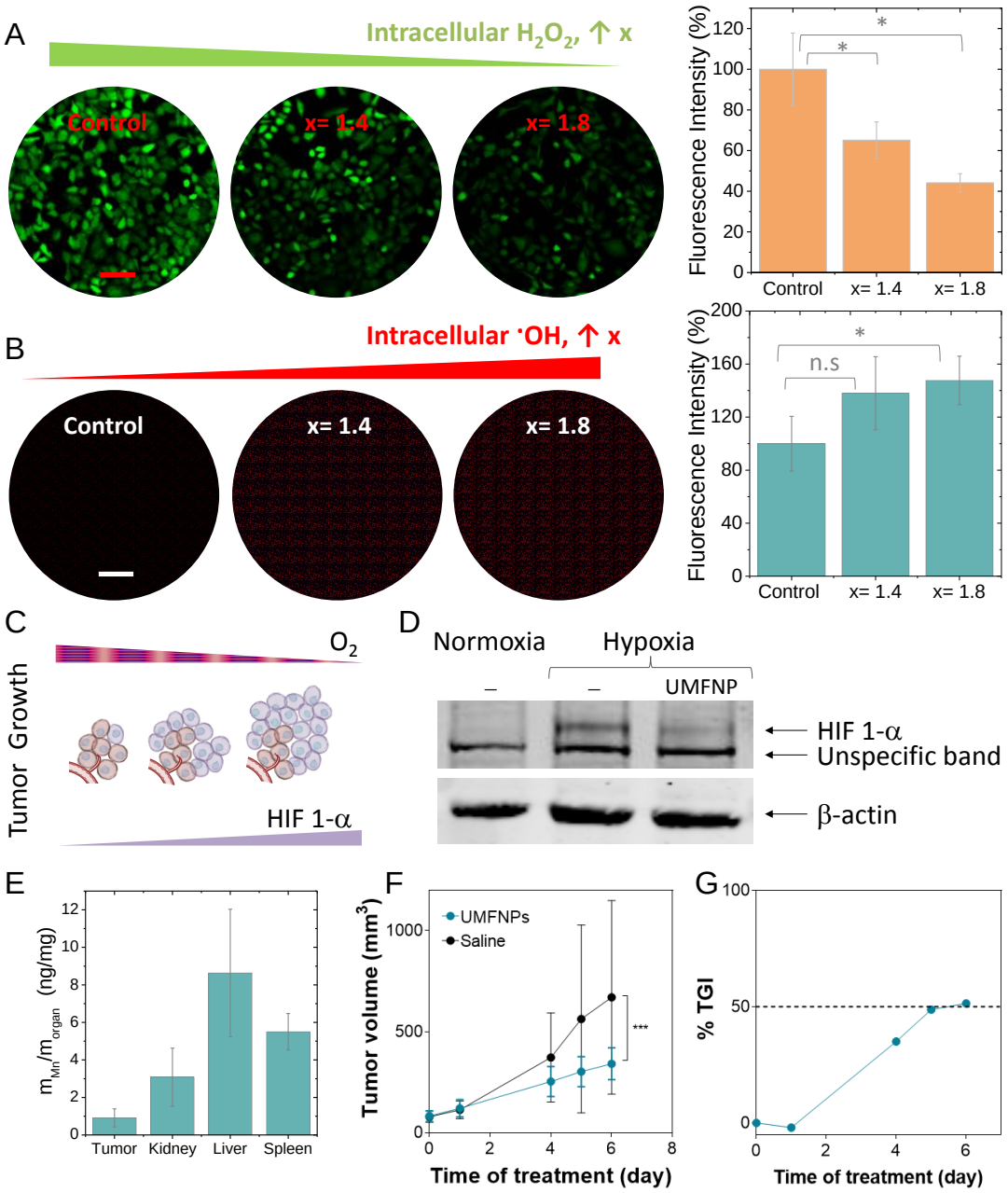

Figure 9. (A) CLSM images and percentage of the fluorescence intensity measurements of A549 cells incubated with the ROS probe DCFH, the intracellular free radical scavenger N-(2-Mercaptopropionyl) glycine and two different UMFNPs with Mn stoichiometry $^{H+}$MnFe12 (*x*= 1.4, *p*= 0.014) and $^{H+}$MnFe13 (*x*=1.8, *p*= 0.001) as compared with control cells incubated with DCFH and (N-(2-Mercaptopropionyl) glycine). (B) CLSM images and percentage of the fluorescence intensity measurements of A549 cells incubated with the hydroxyl radical probe, and two different UMFNPs with Mn stoichiometry x= 1.4 (n.s.) and 1.8 (*p*= 0.013) as compared with control cells incubated with the hydroxyl radical probe. (C) Schematic representation of the inverse

correlation between the molecular oxygen and HIF 1-α concentration with the solid tumor growth. (D) Western blots HIF 1-α reduced expression in A549 cells subjected to hypoxia and treated with UMFNPs. β-actin was used as a loading control. (E) Biodistribution of UMFNPs ($^{H+}$MnFe11) on day 6 after i.v. administration determined by ICP-MS detection of Mn in different organs and the tumor. (F) Temporal evolution of the tumor volume after treatment with UMFNPs (*n*= 6) as compared with the control (*n*= 6) and its corresponding tumor growth inhibition (*TGI*) factor (G).

3. Conclusion

In summary, we successfully synthesized water-soluble citrate coated UMFNPs with well-controlled size and variable Mn doping through a microwave-assisted one-pot method. We generated a series of nanoparticles with tunable magnetic relaxivities, which could be used as T_1 or dual-mode T_1 and T_2 MRI contrast agents depending on the Mn doping level, showing superior MRI contrast versatility and performance than undoped ultrasmall iron oxide NPs. The versatility of our synthetic method allowed multimodal molecular imaging MRI/ PET/CT due to ease core-doping of the UMFNPs with the radioisotope ^{68}Ga. Furthermore, the UMFNPs showed an excellent catalytic activity compared with MFNPs produced with organic or polyol methods. These UMFNPs catalyzed several cycles of H_2O_2 depletion through the Fenton/Haber–Weiss reaction, generating O_2 as the ultimate reaction product. We verified their intracellular catalytic activity and demonstrated their remarkable effect as moderate tumor growth inhibitors in a breast cancer murine model.

In conclusion, herein synthesized UMFNPs exhibit advanced features in multimodal imaging MRI/PET/CT and nanocatalysis. Hence, we envision this multifunctional nanomaterial as a valuable building block for theranostic applications.

4. Experimental Section/Methods

Materials

The chemical reagents iron chloride hexahydrate ($FeCl_3 \cdot 6H_2O$, #236489), manganese dichloride tetrahydrate ($MnCl_2 \cdot 4H_2O$, #244589), citric acid trisodium salt dihydrate ($Na_3C_6H_5O_7 \cdot 2H_2O$, #C3674), and hydrazine monohydrate (64-65%, #207942) were purchased from Sigma-Aldrich and stored in a desiccator. All the syntheses were

carried out with H_2O nanopure water as the solvent. ^{68}Ga ($t_{1/2}$=68 min, β+ emission 89% and EC 11%) was obtained from a $^{68}Ge/^{68}Ga$ generator system (ITG Isotope Technologies, Garching GmbH, Germany) as a 4 mL solution of $^{68}GaCl_3$ (aq) by eluting with HCl 0.05 M (free metal traces).

Synthesis of UMFNPs

To produce UMFNPs with variable Mn and Fe stoichiometries ($Mn_xFe_{3-x}O_4$), different *[$FeCl_3$]/[$MnCl_2$]* precursor ratios were used for the microwave-assisted synthesis as specified in **Table 1**. Briefly, in a 10 mL tube, the correspondent molar ratio of $FeCl_3 \cdot 6H_2O$ (16.9-2.7 mg) and $MnCl_2 \cdot 4H_2O$ (1.5-11.9 mg), from 8.4:1 to 1:6 for UMFNPs with an increasing amount of Mn, was mixed with 20 mg of citric acid trisodium salt dehydrate at a final volume of 2.25 mL. 0.25 mL of hydrazine hydrate was added to the tube before starting the microwave synthesis in all syntheses. The protocol P1 (MnFe1-MnFe7) was carried out using 2.25 mL of nanopure water, while the protocol P2 (MnFe8-$^{H+}$MnFe14) used 2.25 mL of 0.022 M HCl solution. The radiolabeled UMFNPs were produced similarly to P2 but with the HCl solution containing $^{68}GaCl_3$ (0.001mM) traces. The radiolabeling yield was around 50% after 30 minutes from elution. The microwave was programmed with the following steps: 1 min ramping from room temperature to 100 ºC, maintaining 10 min at 100 ºC, and cooling down to room temperature. All UMFNPs were purified with a PD-10 column to eliminate the excess salts and unreacted precursors. For animal administration, 500 µL of 1 mg/mL UMFNP solution was filtered through Amicon 30K, and the retentate was resuspended in 500 µL of saline solution (0.9% NaCl in water).

Magnetic characterization

Sample preparation for magnetic measurements was performed by placing a known volume of each suspension into a cotton wool piece and allowing it to dry at room temperature. The dried wool was then placed inside a gelatin capsule for magnetic characterization. Magnetic measurements were performed in a Quantum Design (USA) MPMS-XL SQUID magnetometer. Field-dependent magnetization was recorded at 300 K in the field ranges between -1600 kA/m and 1600 kA/m. In addition, the temperature dependence of the AC magnetic susceptibility was recorded from 2 to 80 K, at a frequency of 11 Hz and using a magnetic field amplitude of 4.1 Oe.

Relaxometry Measurements

The spin-lattice and spin-spin relaxation times (T_1 and T_2) were measured for five concentrations of each UMFNP sample in a Bruker Minispec MQ60 (Bruker Biospin GmbH) contrast agent analyzer at 1.5 T and 37 ºC. T_1 and T_2 were also measured in a 7 T horizontal bore Bruker Biospec USR 70/30 MRI system (Bruker Biospin GmbH). The relaxivities r_1 and r_2 were plotted against the Mn stoichiometry values and the corresponding synthetic protocol (P1 or P2).

Magnetic Resonance Imaging (MRI)

The MRI scanner was used to determine the feasibility of T_1 and dual-mode T_1/T_2 image contrast of the prepared UMFNPs in mice and the UMFNP biodistribution studies. Animal experiments were conducted at CIC biomaGUNE animal facility, which holds full accreditation from the AAALAC. Our Institutional animal care and ethical committee and local authorities (Diputación Foral de Guipuzcoa, Spain). During the *in vivo* studies, two groups (one for each type of UMFNP) of n= 3 mice were administered intravenously. Female mice C57BL/6JRj were eight weeks old (20 mg body weight), and were obtained from Janvier, France.

Radiolabeling and Positron Emission Tomography (PET)

The reaction to synthesize ^{68}Ga labeled manganese ferrites was similar to the one used for manganese ferrites, except that 1 mL of $^{68}GaCl_3$ (in 0.05M HCl) eluted from the ^{68}Ge/^{68}Ga generator was added to the mixture of iron chloride and manganese chloride precursors and sodium citrate solution. Then, hydrazine hydrate was added, and the reaction was performed in the microwave reaction system at 100 ºC for 10 minutes. After purification through the PD-10 column, to separate free $^{68}Ga^{3+}$ and reactant's waste from labeled UMFNPs, the UMFNPs were filtered (30K Dalton Amicon filters). After that, nanoparticles were resuspended in saline solution (0.9 % NaCl) to be immediately administered intravenously to the mice (100 µl with a radioactivity of about 3 MBq) before performing a PET-scan for a 1h monitoring. *In vivo* PET/CT imaging in mice (eight weeks old C57BL/6JRj female) was performed using a nanoPET/CT small-animal imaging system (Molecubes, Gentt, Belgium). The dynamic PET images were reconstructed in 22 frames of 15 s (4 frames), 30 s (4 frames), 1 min (4 frames), 2 min (4 frames), 5 min (4 frames), 12.5 min (2 frames), taking averaged

data from time points centered at 10, 30, 60 minutes for the data analysis. Quantification for biodistribution of ^{68}Ga manganese ferrites was made with a statistic of n=2.

Catalytic studies

Fenton/Haber-Weiss reaction was studied by determining the temporal decrease of $[H_2O_2]$ catalyzed by UMFNPs and temporal increase of $[O_2]$ concentrations in the reaction solution containing an initial concentration of $[H_2O_2]_=$0.8mM and $[Mn_xFe_{3-x}O_4]$=0.53mM. The temporal measurements of $[H_2O_2]$ were done using a colorimetric enzyme assay with horseradish peroxidase (HRP) and 2,2′-Azino-bis(3-ethylbenzothiazoline-6-sulfonic acid) diammonium salt (ABTS) (H_2O_2 + ABTS $\xrightarrow{HRP}$ $2H_2O$ + oxidized ABTS). The ABTS absorbance was measured at 414 nm, where we did not observe any crosstalk between the ABTS absorption and the absorbance of UMFNPs. We performed the study in 96-well plates where 200 µL of a solution of 0.5 mg/mL HRP and 1mg/mL ABTS were mixed with 10 µL of the reaction solution (H_2O_2/UMFNPs) at different time points. The $[O_2]$ was measured with a PICO2 fiber-optical oxygen meter connected to the oxygen dipping probe OPDIP20 from PyroScience GmbH.

Intracellular catalysis assays

The intracellular ROS depletion was determined using DCFH-DA (2,7-dichlorofluorescein diacetate).[74] A549 lung carcinoma cells were incubated in a 96-well plate ($8x10^3$ cells/well) at 37 °C in a humidified environment containing 5% CO_2. After a night of culture, the cells were treated with 10 µg/mL of UMFNPs with different Mn doping levels for 24h. The medium containing the treatment was then removed and replaced by a serum-free DMEM culture medium. After another 24h, the medium was removed, and the cells were incubated with 20 µM DCFH-DA and 100 µM free radical scavenger (both in serum-free DMEM) for 30 minutes in a dark and humidified atmosphere (37°C, 5% of CO_2). PBS buffer was used again for washing. The fluorescence of each assay was measured with the Confocal Microscope (Zeiss LSM 510) and the microplate reader Thermo Scientific Varioskan® Flash (excitation at 488 nm and emission at 525 nm). Untreated cells were used as a control. To determine the intracellular H_2O_2 fluctuations after UMFNP treatment, we followed the protocol mentioned above but including, before the staining with DCFH-DA, the incubation of the cells with an intracellular free radical scavenger. Briefly, 100 µM of free radical

scavenger (N-(2-Mercaptopropionyl) glycine) in serum-free DMEM was incubated with the cells for 30 min at 37 °C in a humidified atmosphere containing 5% of CO_2. PBS buffer after that for washing and then, we stained the cells with DCFH-DA. According to manufacturer instructions, the Mitochondrial Hydroxyl Radical Detection Assay Kit (Abcam, #ab219931) was used to analyze the hydroxyl radical production. Concisely, A549 cells were cultured and treated as explained above. After 24h with serum-free DMEM culture medium, cells were incubated 1 hour at 37 °C in a humidified atmosphere containing 5% of CO2 with the dye solution of the kit. Then, the solution was removed, and cells were incubated with a serum-free DMEM culture medium. After 1 hour, cells were washed twice with DPBS, and the fluorescence signal was measured (excitation at 540 nm and emission at 590 nm). The fluorescence of each assay was measured with the Confocal Microscope (Zeiss LSM 510) and the microplate reader Thermo Scientific Varioskan® Flash. Untreated cells were used as a control. Western blot analysis of hypoxia-treated cells was performed after seeding A549 cells a day before experimentation in 60-mm-diameter plates. On the day of the experiments, plated cells were introduced into an Invivo2 400 workstation (Ruskinn) set at 1.5 % O_2, 5% CO_2, 37 °C, and incubated for 4h. Protein fraction was extracted in non-reducing Laemmli buffer, and samples run on 10% standard polyacrylamide gel electrophoresis and transferred to PVDF membranes. Polyclonal anti-HIF-1α antibody (#10006421; Cayman Chemicals) and monoclonal anti-β-actin antibody (#A2228; Sigma) were used. Antibody binding was detected by fluorescence with species-specific secondary antibodies labeled with a deep-red fluorophore and visualized on a digital fluorescence image analyzer (ODISSEY).

In vivo tumor growth analysis

All animal procedures conformed to EU Directive 86/609/EEC and Recommendation 2007/526/EC regarding the protection of animals used for experimental and other scientific purposes, enforced in Spanish law under Real Decreto 1201/2005. Twelve C57BL/6JOlaHsd female mice were purchased from Harlan Laboratories and housed under standard conditions. At twelve weeks old, $1 \cdot 10^6$ murine breast cancer cells (E0771 cells, CH3 BioSystems, LLC) resuspended in 50 µL of PBS 1x, and Matrigel® were subcutaneously injected on their second right mammary gland. 80 ± 25 mm^3 tumors were established before randomization into groups (6 mice each). 150 µL of a 6 mg/mL solution of UMFNPs ($^{H+}$MnFe11, x=1) or vehicle (0.9% Saline

Solution) was administered intravenously into the tail vein. Body weights were periodically determined. Tumor volumes ($V= [length \times (width)^2]/2$) were monitored using Vernier calipers in a blinded manner. The tumor growth inhibition (*%TGI*) was determined using the following formula: $\%TGI= [1 - (T_t/T_0)/(C_t/C_0)] \times 100$; where T is the mean tumor volume in the treatment group at a single time-point and C is the mean tumor volume at that exact point in the control group. Mice were prematurely euthanized when their tumor volume reached 1000 mm^3. The rest of the mice were sacrificed on day 6 after UMFNP or vehicle injection. Tumors were harvested and weighed. Then, tumors, liver, spleen, and kidneys, were frozen for further biodistribution analysis by ICP-MS and molecular analysis such as PCR.

For more details regarding the experimental section and additional results, the reader is referred to the Supporting Information.

Supporting Information

Supporting Information is available from the Wiley Online Library or the author.

Acknowledgments

SCR is supported by the grant PID2019-106139RA-100 funded by MCIN. JRC is supported by grants from the Ministerio de Economía, Industria y Competitividad (MEIC) (SAF2017-84494-C2-R). JRC received funding from the BBVA Foundation (PR [18]_BIO_IMG_0008) and La Caixa (HR18-00052). YFA received funding from the Santander-Universidad Zaragoza Fellowship program. LG acknowledges financial support from the Ramón y Cajal program (RYC-2014-15512). CIC biomaGUNE is supported by the Maria de Maeztu Units of Excellence Program from the Spanish State Research Agency (MDM-2017-0720). The authors would like to acknowledge the use of Servicio General de Apoyo a la Investigación-SAI, Universidad de Zaragoza. HG is supported by the Ligue contre le Cancer (CD16, CD17) and Région Nouvelle Aquitaine (Projet "Nanovect"). JAE is supported by RTI2018-099357-B-I00, HFSP (RGP0016/2018), CIBERFES16/10/00282 and RED2018-102576-T. The CNIC is supported by the Pro-CNIC Foundation and by the Severo Ochoa of Excellence Program.

Received: ((will be filled in by the editorial staff))
Revised: ((will be filled in by the editorial staff))
Published online: ((will be filled in by the editorial staff))

References

1. Kim, J.; Kim, H. Y.; Song, S. Y.; Go, S.-h.; Sohn, H. S.; Baik, S.; Soh, M.; Kim, K.; Kim, D.; Kim, H.-C.; Lee, N.; Kim, B.-S.; Hyeon, T., *ACS Nano* **2019,** *13* (3), 3206.

2. Miao, Y.; Xie, Q.; Zhang, H.; Cai, J.; Liu, X.; Jiao, J.; Hu, S.; Ghosal, A.; Yang, Y.; Fan, H., *Theranostics* **2019,** *9*, 1764.

3. Kim, J.; Cho, H. R.; Jeon, H.; Kim, D.; Song, C.; Lee, N.; Choi, S. H.; Hyeon, T., *J. Am. Chem. Soc.* **2017,** *139*, 10992.

4. Pardo, A.; Pelaz, B.; Gallo, J.; Bañobre-López, M.; Parak, W. J.; Barbosa, S.; del Pino, P.; Taboada, P., *Chem. Mater.* **2020,** *32*, 2220.

5. Yin, S.-Y.; Song, G.; Yang, Y.; Zhao, Y.; Wang, P.; Zhu, L.-M.; Yin, X.; Zhang, X.-B., *Adv. Funct. Mater.* **2019,** *29*, 1901417.

6. Han, J.; Yoon, J., *ACS Appl. Bio Mater.* **2020,** *3*, 7344.

7. Szatrowski, T. P.; Nathan, C. F., *Cancer Res.* **1991,** *51*, 794.

8. Jernigan, N.; Naik, J.; Weise-Cross, L.; Detweiler, N.; Herbert, L.; Yellowhair, T.; Resta, T., *PLOS ONE* **2017,** *12*, e0180455.

9. Halliwell, B.; Clement, M. V.; Long, L. H., *FEBS letters* **2000,** *486*, 10.

10. Wu, H.; Liao, H.; Li, F.; Lee, J.; Hu, P.; Shao, W.; Li, X.; Ling, D., *Nano Select* **2020,** *1*, 285.

11. Ranji-Burachaloo, H.; Gurr, P. A.; Dunstan, D. E.; Qiao, G. G., *ACS Nano* **2018,** *12*, 11819.

12. Yang, K.; Yue, L.; Yu, G.; Rao, L.; Tian, R.; Wei, J.; Yang, Z.; Sun, C.; Zhang, X.; Xu, M.; Yuan, Z.; Chen, X.; Wang, R., *Biomaterials* **2021,** *275*, 120822.

13. Yang, K.; Yu, G.; Tian, R.; Zhou, Z.; Deng, H.; Li, L.; Yang, Z.; Zhang, G.; Liu, D.; Wei, J.; Yue, L.; Wang, R.; Chen, X., *Adv. Funct. Mater.* **2021,** *31*, 2008078.

14. Lasheras, X.; Insausti, M.; de la Fuente, J. M.; Gil de Muro, I.; Castellanos-Rubio, I.; Marcano, L.; Fernández-Gubieda, M. L.; Serrano, A.; Martín-Rodríguez, R.; Garaio, E.; García, J. A.; Lezama, L., *Dalton Trans.* **2019,** *48*, 11480.

15. Lu, J.; Ma, S. L.; Sun, J. Y.; Xia, C. C.; Liu, C.; Wang, Z. Y.; Zhao, X. N.; Gao, F. B.; Gong, Q. Y.; Song, B.; Shuai, X. T.; Ai, H.; Gu, Z. W., *Biomaterials* **2009,** *30*, 2919.

16. Pernia Leal, M.; Rivera-Fernández, S.; Franco, J. M.; Pozo, D.; de la Fuente, J. M.; García-Martín, M. L., *Nanoscale* **2015,** *7*, 2050.

17. Tong, S.; Quinto, C. A.; Zhang, L.; Mohindra, P.; Bao, G., *ACS Nano* **2017,** *11*, 6808.

18. Yang, K.; Liu, Y.; Liu, Y.; Zhang, Q.; Kong, C.; Yi, C.; Zhou, Z.; Wang, Z.; Zhang, G.; Zhang, Y.; Khashab, N. M.; Chen, X.; Nie, Z., *J. Am. Chem. Soc.* **2018,** *140*, 4666.

19. Lu, Y.; Xu, Y.-J.; Zhang, G.-b.; Ling, D.; Wang, M.-q.; Zhou, Y.; Wu, Y.-D.; Wu, T.; Hackett, M. J.; Hyo Kim, B.; Chang, H.; Kim, J.; Hu, X.-T.; Dong, L.; Lee, N.; Li, F.; He, J.-C.; Zhang, L.; Wen, H.-Q.; Yang, B.; Hong Choi, S.; Hyeon, T.; Zou, D.-H., *Nat. Biomed. Eng.* **2017,** *1*, 637.

20. Ni, D.; Bu, W.; Ehlerding, E. B.; Cai, W.; Shi, J., *Chem. Soc. Rev.* **2017,** *46*, 7438.

21. Shin, T.-H.; Choi, J.-s.; Yun, S.; Kim, I.-S.; Song, H.-T.; Kim, Y.; Park, K. I.; Cheon, J., *ACS Nano* **2014,** *8*, 3393.

22. Thapa, B.; Diaz-Diestra, D.; Santiago-Medina, C.; Kumar, N.; Tu, K.; Beltran-Huarac, J.; Jadwisienczak, W. M.; Weiner, B. R.; Morell, G., *ACS Appl. Bio Mater.* **2018,** *1*, 79.

23. Fu, Y.; Li, X.; Chen, H.; Wang, Z.; Yang, W.; Zhang, H., *ACS Appl. Bio Mater.* **2019,** *2*, 3613.

24. García-Soriano, D.; Amaro, R.; Lafuente-Gómez, N.; Milán-Rois, P.; Somoza, Á.; Navío, C.; Herranz, F.; Gutiérrez, L.; Salas, G., *J. Colloid Interface Sci* **2020,** *578*, 510.

25. Colombo, M.; Carregal-Romero, S.; Casula, M. F.; Gutierrez, L.; Morales, M. P.; Bohm, I. B.; Heverhagen, J. T.; Prosperi, D.; Parak, W. J., *Chem. Soc. Rev.* **2012,** *41*, 4306.

26. Caruntu, D.; Caruntu, G.; Chen, Y.; O'Connor, C. J.; Goloverda, G.; Kolesnichenko, V. L., *Chem. Mater.* **2004,** *16*, 5527.

27. Hu, X.; Yu, J. C.; Gong, J.; Li, Q.; Li, G., *Adv. Mater.* **2007,** *19*, 2324.

28. Carenza, E.; Barceló, V.; Morancho, A.; Montaner, J.; Rosell, A.; Roig, A., *Acta Biomater.* **2014,** *10*, 3775.

29. Pellico, J.; Ruiz-Cabello, J.; Fernández-Barahona, I.; Gutiérrez, L.; Lechuga-Vieco, A. V.; Enríquez, J. A.; Morales, M. P.; Herranz, F., *Langmuir* **2017,** *33*, 10239.

30. Pellico, J.; Ruiz-Cabello, J.; Saiz-Alía, M.; Rosario, G.; Caja, S.; Montoya, M.; Fernández de Manuel, L.; Morales, M. P.; Gutiérrez, L.; Galiana, B.; Enríquez, J. A.; Herranz, F., *Contrast Media Mol. Imaging* **2016,** *11*, 203.

31. Adrover, J. M.; Pellico, J.; Fernández-Barahona, I.; Martín-Salamanca, S.; Ruiz-Cabello, J.; Hidalgo, A.; Herranz, F., *Nanoscale* **2020,** *12*, 22978.

32. Wiogo, H.; Lim, M.; Munroe, P.; Amal, R., *Cryst. Growth Des.* **2011,** *11*, 1689.

33. Szczerba, W.; Żukrowski, J.; Przybylski, M.; Sikora, M.; Safonova, O.; Shmeliov, A.; Nicolosi, V.; Schneider, M.; Granath, T.; Oppmann, M.; Straßer, M.; Mandel, K., *Phys. Chem. Chem. Phys.* **2016,** *18*, 25221.

34. Baig, M. M.; Yousuf, M. A.; Agboola, P. O.; Khan, M. A.; Shakir, I.; Warsi, M. F., *Ceram. Int.* **2019,** *45*, 12682.

35. Jolivet, J.-P.; Chanéac, C.; Tronc, E., *Chem. Comm.* **2004,** 481.

36. Lim, M.; Chiang, K.; Amal, R., *J. Photoch. Photobio.* **2006,** *183*, 126.

37. Thanh, N. T. K.; Maclean, N.; Mahiddine, S., *Chem. Rev.* **2014,** *114*, 7610.

38. Fernández-Barahona, I.; Gutiérrez, L.; Veintemillas-Verdaguer, S.; Pellico, J.; Morales, M. d. P.; Catala, M.; del Pozo, M. A.; Ruiz-Cabello, J.; Herranz, F., *ACS Omega* **2019,** *4*, 2719.

39. Zhang, H.; Li, L.; Liu, X. L.; Jiao, J.; Ng, C.-T.; Yi, J. B.; Luo, Y. E.; Bay, B.-H.; Zhao, L. Y.; Peng, M. L.; Gu, N.; Fan, H. M., *ACS Nano* **2017,** *11*, 3614.

40. Testa-Anta, M.; Ramos-Docampo, M. A.; Comesaña-Hermo, M.; Rivas-Murias, B.; Salgueiriño, V., *Nanoscale Adv.* **2019,** *1*, 2086.

41. Otero-Lorenzo, R.; Fantechi, E.; Sangregorio, C.; Salgueiriño, V., *Chem. Eur. J.* **2016,** *22*, 6666.

42. Chamritski, I.; Burns, G., *J. Phys. Chem.* **2005,** *109*, 4965.

43. Pereira, C.; Pereira, A. M.; Fernandes, C.; Rocha, M.; Mendes, R.; Fernández-García, M. P.; Guedes, A.; Tavares, P. B.; Grenèche, J.-M.; Araújo, J. P.; Freire, C., *Chem. Mater.* **2012,** *24*, 1496.

44. Julien, C. M.; Massot, M.; Poinsignon, C., *Spectrochim. Acta A* **2004,** *60*, 689.

45. Aslibeiki, B.; Kameli, P.; Ehsani, M. H., *Ceram. Int.* **2016,** *42*, 12789.

46. Cornell, R. M.; Schwertmann, H. C. U., The Iron Oxides: Structure, Properties, Reactions, Occurences and Uses, Second Edition. In *The Iron Oxides: Structure, Properties, Reactions, Occurences and Uses*, Wiley-VCH, Ed. Wiley-VCH: 2003; pp 1.

47. Li, D.; Yun, H.; Diroll, B. T.; Doan-Nguyen, V. V. T.; Kikkawa, J. M.; Murray, C. B., *Chem. Mater.* **2016,** *28*, 480.

48. Zyuzin, M. V.; Honold, T.; Carregal-Romero, S.; Kantner, K.; Karg, M.; Parak, W. J., *Small* **2016,** *12*, 1723.

49. Wright, A. K.; Thompson, M. R., *Biophys. J.* **1975,** *15*, 137.

50. Dominguez-Medina, S.; Blankenburg, J.; Olson, J.; Landes, C. F.; Link, S., *ACS Sustain. Chem. Eng.* **2013,** *1*, 833.

51. Abdelwahed, W.; Degobert, G.; Stainmesse, S.; Fessi, H., *Adv. Drug Deliv. Rev.* **2006,** *58*, 1688.

52. Rohrer, M.; Bauer, H.; Mintorovitch, J.; Requardt, M.; Weinmann, H. J., *Investig. Radiol.* **2005,** *40*, 715.

53. Dobrovolskaia, M. A.; Clogston, J. D.; Neun, B. W.; Hall, J. B.; Patri, A. K.; McNeil, S. E., *Nano Letters* **2008,** *8*, 2180.

54. Feng, Q.; Liu, Y.; Huang, J.; Chen, K.; Huang, J.; Xiao, K., *Sci. Rep.* **2018,** *8*, 2082.

55. Costa, R. C. C.; Lelis, M. F. F.; Oliveira, L. C. A.; Fabris, J. D.; Ardisson, J. D.; Rios, R. R. V. A.; Silva, C. N.; Lago, R. M., *J. Hazard. Mater.* **2006,** *129*, 171.

56. Ramankutty, C. G.; Sugunan, S., *Appl. Catal. A: Gen.* **2001,** *218*, 39.

57. Chen, W.; Chen, X. Y.; Wang, Y.; Wang, H. Y.; Zhou, W. J.; Yu, T., *J. Cardiovasc. Pharmacol.* **2019,** *73*, 265.

58. Zhang, C.; Li, J.; Lu, C.; Yang, T.; Zhao, Y.; Teng, L.; Yang, Y.; Song, G.; Zhang, X.-B., *CCS Chemistry* **2020,** *0*.

59. Phelps, M. E., *Proc. Natl. Acad. Sci. U S A* **2000,** *97*, 9226.

60. Pellico, J.; Lechuga-Vieco, A. V.; Almarza, E.; Hidalgo, A.; Mesa-Nuñez, C.; Fernández-Barahona, I.; Quintana, J. A.; Bueren, J.; Enríquez, J. A.; Ruiz-Cabello, J.; Herranz, F., *Sci. Rep.* **2017,** *7*, 13242.

61. Alexis, F.; Pridgen, E.; Molnar, L. K.; Farokhzad, O. C., *Mol. Pharm.* **2008,** *5*, 505.

62. Yu, M.; Zheng, J., *ACS Nano* **2015,** *9*, 6655.

63. Muz, B.; de la Puente, P.; Azab, F.; Azab, A. K., *Hypoxia (Auckl)* **2015,** *3*, 83.

64. Valdés-Solís, T.; Valle-Vigón, P.; Álvarez, S.; Marbán, G.; Fuertes, A. B., *Catal. Comm.* **2007,** *8*, 2037.

65. Costa, R. C. C.; Lelis, M. d. F. F.; Oliveira, L. C. A.; Fabris, J. D.; Ardisson, J. D.; Rios, R. R. V. A.; Silva, C. N.; Lago, R. M., *Catal. Comm.* **2003,** *4*, 525.

66. Li, M.; Gao, Q.; Wang, T.; Gong, Y.-S.; Han, B.; Xia, K.-S.; Zhou, C.-G., *Mater. Des.* **2016,** *97*, 341.

67. Mursaleen, L.; Noble, B.; Chan, S. H. Y.; Somavarapu, S.; Zariwala, M. G., *Antioxidants* **2020,** *9*, 600.

68. Halliwell, B.; Adhikary, A.; Dingfelder, M.; Dizdaroglu, M., *Chem. Soc. Rev.* **2021**.

69. Petrova, V.; Annicchiarico-Petruzzelli, M.; Melino, G.; Amelio, I., *Oncogenesis* **2018,** *7*, 10.

70. Semenza, G. L., *Trends Mol. Med.* **2002,** *8*, S62.

71. Boedtkjer, E.; Pedersen, S. F., *Annu. Rev. Physiol.* **2020,** *82*, 103.

72. Johnstone, C. N.; Smith, Y. E.; Cao, Y.; Burrows, A. D.; Cross, R. S.; Ling, X.; Redvers, R. P.; Doherty, J. P.; Eckhardt, B. L.; Natoli, A. L.; Restall, C. M.; Lucas, E.; Pearson, H. B.; Deb, S.; Britt, K. L.; Rizzitelli, A.; Li, J.; Harmey, J. H.; Pouliot, N.; Anderson, R. L., *Dis. Model Mech.* **2015,** *8*, 237.

73. Shi, Y.; van der Meel, R.; Chen, X.; Lammers, T., *Theranostics* **2020,** *10*, 7921.

74. Eruslanov, E.; Kusmartsev, S., *Methods Mol. Biol.* **2010,** *594*, 57.